UNIVERSITÉ DENIS DIDEROT

Paris VII

THÈSE

presentée par

Mohammad Ijaz AYYAZ

pour obtenir

le titre de Docteur de l'Université de Paris VII

(Spécialité Physique et Technologie des Grands Instruments)

SUJET

Measurement of the Proton Structure Function $F_2(x, Q^2)$ at low x and low Q^2 with the H1 Detector at HERA.

Soutenue le 24 juin 1999 devant le jury composé de:

M.	Banner	
U.	Bassler	
M.-C.	Cousinou	
C.	Guyot	Rapporteur
M.	Jaffre	Rapporteur
F.	Vannucci	Président

Resumé

Dans cette thèse la mesure de la fonction de structure du proton $F_2(x, Q^2)$ est présentée, effectuée avec les données prises en 1995 par l'expérience H1 auprès du collisionneur HERA dans le domaine cinématique de $10^{-5} \leq x \leq 10^{-2}$ et de $0.85 \leq Q^2 \leq 20\ GeV^2$. Cette mesure est faite avec les premières données prises après que les détecteurs "arrières" de H1 aient été améliorés, avec l'installation d'un calorimètre de type SpaCal, et l'adjonction d'une chambre à dérive à 4 plans, la BDC. Ces deux détecteurs et leurs performances sont décrits en détail en parallèle avec les autres sous-détecteurs utilisés dans l'analyse. De nouvelles techniques d'analyse concernant la calibration, la reconstruction cinématique et la suppression du bruit dans le SpaCal sont présentées. Les résultats obtenus sur F_2 sont en bon accord avec les mesures précédentes faites à HERA, et ont une précision meilleure dans la région de Q^2 entre 3 et 10 GeV^2, dans laquelle le régime perturbatif de la Chromodynamique Quantique est atteint. La validité des équations d'évolution à l'ordre "Next-to-Leading" de la QCD est montré.

Abstract

In this thesis the measurement of the proton structure function $F_2(x, Q^2)$ is presented in the kinematic domain of $10^{-5} \leq x \leq 10^{-2}$ and of $0.85 \leq Q^2 \leq 20\ GeV^2$ with the H1 experiment at the electron-proton collider HERA using data taken during the year 1995. This measurement is done with the first H1 data after the "backward" detectors were upgraded with a new calorimeter of the SpaCal type, and a new drift chamber (BDC) in front of it. Both these detectors and their performances are described in detail along with the other detector components used in the analysis. New analysis techniques are presented, concerning the calibration, the kinematic reconstruction and the noise suppression in the SpaCal calorimeter. The F_2 results are in good agreement with previous HERA data, and have an improved precision in the region of Q^2 between 3 and 10 GeV^2, in which the perturbative regime of QCD is reached. The validity of Next to Leading Order QCD to explain the rise at low x of the F_2 proton cross-section is shown.

Introduction

The most direct way to study the structure of the nucleon consists in breaking up the proton by scattering energetic leptons off it. This type of interaction, called Deep Inelastic Scattering (DIS), revealed about thirty years ago the compositeness of the proton, and in the following its constituents: quarks and gluons and their interaction, described by the theory of QuantumChromoDynamics (QCD). Until the early nineties, DIS experiments were performed in the fixed target mode by shooting electron, muon or neutrino beams on Hydrogen, Deuterium or, especially for neutrino scattering, on heavy targets like carbon or even lead, which allow not only to study the proton structure, but also the neutron structure and the different effects of their binding in the nucleon. From double differential cross-section measurements of these lepton-nucleon interactions, structure functions can be determined, which can be interpreted as the sum of the various quark densities in the nucleon and be linked by their evolution in the phase space to the gluon density. Although the evolution of the parton densities can be established in different models in one dimension of the phase space, precise experimental measurements are necessary to determine their shape and to verify the validity of different assumptions made by the various models.

With HERA (Hadron-Electron Ring Accelerator) at DESY (Deutsches Electronen SYnchrotron) a collider of leptons and hadrons was built for the first time: in 1992 the first collisions between 26.7 GeV electrons and 820 GeV hadrons were performed and observed by the H1 and ZEUS experiments. The increase of the center of mass energy $\sqrt{s} \simeq 300\ GeV$, obtained by the collider mode, presents an important increase in the kinematic region accessible for the proton structure studies. Figure 0.1 shows a comparison of the accessible regions between HERA and various fixed target experiments in the two kinematic variables, mostly used for the description of the proton structure: x, the fractional momentum of the struck quark in the infinite momentum frame of the proton, and Q^2, the squared momentum transfer between the scattered lepton and the proton. HERA allowed to extend the measurement of the proton structure towards low x and at high Q^2, by roughly three orders of magnitude. In 1992, the first year of operation of HERA, the rise of the structure function F_2 with decreasing x was established and related to an increase of the gluon density. In the following years, the increase in luminosity allowed for a more precise quantification of this effect, as well as for the study of consequent predictions for exclusive processes, as for example the contribution from charm production to the structure function.

In 1995, the H1 collaboration replaced detector components in the backward re-

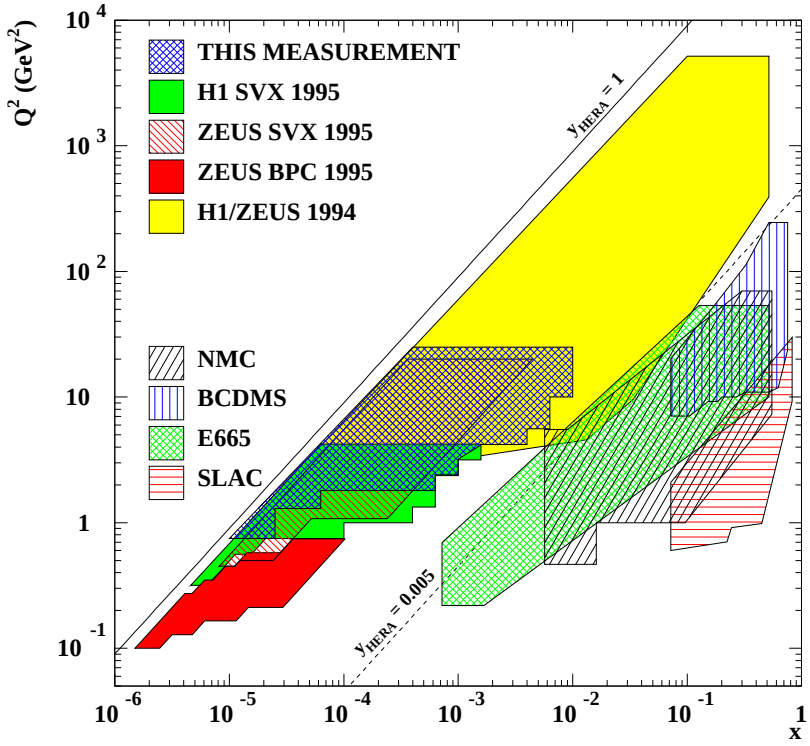

Figure 0.1: *Kinematic plane of the accessible region for Proton Structure Function measurements comparing HERA and various fixed target experiments.*

gion [1], which is the most relevant region for the detection of the scattered electron at low x and low Q^2, by a Backward Drift Chamber (BDC) and a SpaCal Calorimeter, allowing for an extension of the measurable kinematic region towards lower x and lower Q^2. Most of the 1995 running was devoted to the commissioning of these new subdetectors, but enough data was taken in order to improve the previous measurements in the region of Q^2 between 1 and 10 GeV^2, which will be described in this thesis. A period of data taking was devoted in 1995 to explore the region down to $Q^2 = 0.35\ GeV^2$, by shifting the interaction vertex in the proton beam direction. These two measurements allowed for a more precise description of the transition region between real photon exchange (photoproduction) and virtual photon exchange (DIS), in which the breakdown of the validity of perturbative developments of QCD is expected.

After a brief description of the theoretical background of Deep Inelastic Scattering in chapter 1, the experimental setup is presented in chapter 2. The various steps of the event selection (chapter 3), the calibration and correction procedures used for the cross-section measurement (chapter 4) are discussed. The chapter 5 is devoted to the F_2 measurement and to a brief interpretation of the results.

[1] At HERA, the positive z-axis is defined in the direction of the proton beam.

.

Contents

Chapter 1

Deep Inelastic Scattering and F_2

Deep inelastic scattering (DIS) of electrons off protons has revealed in the late sixties the partonic structure of the proton [1, 2, 3]: the scattering can in fact be thought of as between the electron and one of the constituents of the proton. The structure of the proton is translated into measurable quantities called the structure functions. From these functions one can study different properties as the composition and the behaviour of the proton constituents. QuantumChromoDynamics (QCD) describes the so called "strong interaction" among these constituents. The perturbative development of QCD (pQCD) can be tested by measuring the structure functions in different kinematic regions and studying their variations.

This chapter presents the definition of the structure functions from the cross section and their interpretation in the Quark Parton Model (QPM) and in pQCD. In section 1.1 the event kinematics are defined. In section 1.2 the structure functions and their relation to the cross section are presented. In section 1.3 the interpretation of the structure functions in the framework of the QPM is developed. Section 1.4 establishes the DGLAP evolution equations of the parton densities in the QCD frame. In section 1.5 the QCD fits to the structure functions are discussed along with parameterization schemes of the parton densities. In section 1.6 models describing the transition between photoproduction and DIS are presented.

1.1 The Kinematics of Deep Inelastic Scattering

The deep inelastic scattering of an electron off a proton can be described at the lowest order by the diagram in figure 1.1. An incident electron of 4-momentum $k(E, 0, 0, \sqrt{E^2 - m_e^2})$ interacts with a proton of 4-momentum $p(E_p, 0, 0, -\sqrt{E_p^2 - m_p^2})$. At HERA, the energy of the incoming electron and proton is $E = 27.6\ GeV$ and $E_p = 820\ GeV$ respectively, so we can neglect the masses of the particles in the following. In neutral current events the electron and the proton exchange a boson γ or Z^o with 4-momentum $q(\nu, \vec{q})$. After the scattering, the 4-momentum of the electron can be written as $k'(E', \vec{k'})$, while the proton generally breaks up in several particles, forming the hadronic final state X. In charged current events, the outgoing lepton is a neutrino and the exchanged particle a charged W boson.

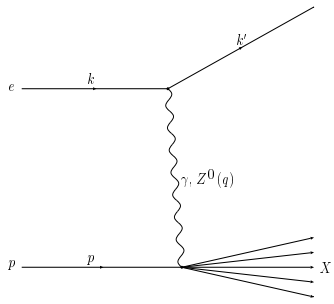

Figure 1.1: *Diagram for DIS ep-scattering.*

We define three Lorenz invariant quantities Q^2, x and y in order to describe the interaction, as

$$Q^2 = -q^2 = -(k - k')^2 \tag{1.1}$$

$$x = Q^2/2p.q \tag{1.2}$$

$$y = p.q/p.k \tag{1.3}$$

In DIS, the boson propagator is always space-like, therefore, we define a positive quantity Q^2, the squared momentum transfer, as the virtuality of the exchanged boson. As the Z and the W bosons are massive, their exchange is only relevant at large Q^2 (of the order of $M^2 \sim 10^4\ GeV^2$) and not treated in the following, since the measurement takes place at $Q^2 \sim 10\ GeV^2$. The influence of the Z exchange on the F_2 structure function is about 1% at $Q^2 \sim 1000 GeV^2$. x is the Bjorken variable, which can be interpreted in the frame of infinite momentum of the proton, as the fractional proton momentum carried by the struck quark. The third quantity y, usually termed as inelasticity, is the fractional electron energy carried by the virtual photon in the proton rest frame. Further two useful quantities are defined as,

$$s = (k + p)^2 \tag{1.4}$$

$$W^2 = (q + p)^2 \tag{1.5}$$

s, the total ep center of mass energy squared, is characteristic of the accelerator and the hadronic final state mass W, is the total $\gamma^* p$ center of mass energy. Using the 4-momentum of the incoming particles and neglecting the masses of the electron m_e and the proton m_p, s becomes

$$s = 4EE_p \tag{1.6}$$

leading to a center of mass energy $\sqrt{s}$ of about 300 GeV which is related to the other kinematic variables by

$$Q^2 = sxy \tag{1.7}$$

Within this approximation we obtain W^2 as,

$$W^2 = \frac{(1 - x)}{x} Q^2 \tag{1.8}$$

1.2 The Inclusive Cross-Section and the Structure Functions

The double differential cross section for DIS of non-polarized electrons and protons (ep) exchanging a photon is given by [4, 5]

$$\frac{d^2\sigma}{d\Omega dE'} = \frac{\alpha^2}{Q^4}(\frac{E'}{E})L^{\mu\nu}W_{\mu\nu} \tag{1.9}$$

Here $\alpha = \frac{e^2}{4\pi}$ is the electromagnetic coupling constant. The angular phase space of the scattered electron is described by $d\Omega$, i.e.

$$d\Omega = \sin\theta d\theta d\phi \tag{1.10}$$

The leptonic tensor $L^{\mu\nu}$ describes the electron-photon interaction and is completely known following the point-like nature of the electron. It is given by

$$L_{\mu\nu} \equiv \frac{1}{2}tr(\not{k}'\gamma_\mu \not{k}\gamma_\nu) = 2(k_\mu k'_\nu + k'_\mu k_\nu + \frac{q^2}{2}g_{\mu\nu}) \tag{1.11}$$

for an electromagnetic interaction of a non-polarized spin 1/2 particle. Here γ are the four 4×4 Dirac matrices and $g_{\mu\nu}$ is the completely symmetric tensor. The hadronic tensor $W_{\mu\nu}$ describes the boson-proton interaction. Its form is not known exactly, since the proton has a complex structure. It is given in terms of the hadronic current operators $J_\mu(x)$ as,

$$W_{\mu\nu}(p,q) = \frac{1}{4m_p}\int \frac{d^4x}{2\pi}e^{iq.x} < p|J_\mu(x)J_\nu(0)|p > \tag{1.12}$$

with the proton mass m_p. Using the arguments of Lorenz invariance and current conservation, the tensor can be constructed in the most generalized form, from two available 4-vectors p^μ and q^ν, the symmetric tensor $g^{\mu\nu}$, the asymmetric tensor $\epsilon^{\mu\nu\alpha\beta}$ and scalars functions which only depend upon the independent scalar variables $p \cdot q$ and Q^2. This leads to the following expression,

$$W_{\mu\nu}(p,q) = F_1(x,Q^2)(-g_{\mu\nu} - \frac{q_\mu q_\nu}{Q^2}) + F_2(x,Q^2)\frac{P_\mu P_\nu}{p.q} - iF_3(x,Q^2)\epsilon_{\mu\nu\alpha\beta}\frac{p^\alpha q^\beta}{p.q} \tag{1.13}$$

With a modified vector P_μ defined as,

$$P^\mu \equiv p^\mu + \frac{p \cdot q}{Q^2}q^\mu \tag{1.14}$$

The hadronic tensor contains three unknown scalar functions F_1, F_2 and F_3, termed as structure functions. At large Q^2 ($\sqrt{Q^2} >> 1/D$, with the proton size $D \sim 3GeV^{-1}$), the structure functions F_1 and F_2 describe the density of the constituents (called partons, assuming that the proton has a substructure) and their momentum inside the proton [6]. They correspond to the elastic form factors in the low Q^2 limit.

The F_3 structure function is vanishing for purely electromagetic interactions, as the leptonic tensor does not contain an asymetric component, which must be added when taking into account the Z exchange, where also the weak contribution to F_2 must be considered [7]. Substituting these tensors in the cross section expression, one arrives at

$$\frac{d^2\sigma^{e^{\pm}p}}{dxdQ^2} = \frac{4\pi\alpha^2}{xQ^4}[y^2xF_1(x,Q^2) + (1-y)F_2(x,Q^2)] \tag{1.15}$$

Considering only the virtual photon exchange, the process $ep \to e'X$ can be factorized in two parts $e \to e'\gamma^*$ and $\gamma^*p \to X$. The aim of using the electron as a beam is in fact to get a virtual photon which probes the structure of the proton. The total cross section for the later process is:

$$\sigma^{tot}(\gamma^*p \to X) = \sum_{\lambda} \frac{8\pi^2\alpha M}{W^2 - M^2}\epsilon_{\lambda}^{\mu *}\epsilon_{\lambda}^{\nu}W_{\mu\nu} \tag{1.16}$$

with ϵ_{λ}^{μ} being the polarization vector of photon and λ its helicity which contrary to a real photon can have both longitudinal ($\lambda = 0$) and transverse ($\lambda = \pm 1$) components. The cross-section can be decomposed as

$$\sigma^{tot} = \sigma_T + \sigma_L \tag{1.17}$$

Putting the explicit form of the polarization vectors and substituting the expression of $W_{\mu\nu}$ from equation 1.13, the two parts can be written in terms of structure functions,

$$\sigma_T = \sigma_{\lambda=+1} + \sigma_{\lambda=-1} = \frac{4\pi^2\alpha}{Q^2(1-x)} \cdot 2xF_1(x,Q^2) \tag{1.18}$$

$$\sigma_L = \sigma_{\lambda=0} = \frac{4\pi^2\alpha}{Q^2(1-x)}[F_2(x,Q^2) - 2xF_1(x,Q^2)] \tag{1.19}$$

Based on the helicity of the virtual photon, the longitudinal and transverse structure functions of the proton are defined as,

$$F_L(x,Q^2) \equiv F_2(x,Q^2) - 2xF_1(x,Q^2) \tag{1.20}$$

$$F_T(x,Q^2) \equiv 2xF_1(x,Q^2) \tag{1.21}$$

1.3 The Quark Parton Model and the Quark Momentum Distribution Functions

In a system in which the proton is moving with an infinite momentum, the partons find no time available for mutual interactions during the scattering and the proton can be simply pictured as being made up of free massless partons [6]. This picture is called the Quark-Parton Model (QPM), which leads to an simple interpretation of the structure functions in terms of parton densities. Using the Feynman rules,

the double differential cross section for an electromagnetic interaction between an electron and the i^{th} pointlike parton of spin 1/2, called quark, carrying a momentum fraction ω $(0 \leq \omega \leq 1)$ of the proton is given by

$$\frac{d^2\sigma_i}{dxdQ^2} = \frac{4\pi\alpha^2}{Q^4} e_i^2 \frac{1}{2}[1 + (1-y)^2]\delta(x-\omega) \tag{1.22}$$

The presence of the Dirac function δ in this cross section, gives a physical meaning to the variables x, as being the momentum fraction carried by the struck quark. If $d\omega f_i(\omega)$ is the probability of finding the i^{th} struck quark in the proton carrying a momentum fraction between ω and $\omega + d\omega$, then the total electron proton scattering cross section will be:

$$\frac{d^2\sigma}{dxdQ^2} = \sum_i \int_0^1 d\omega f_i(\omega) \frac{d^2\sigma_i}{dxdQ^2} \tag{1.23}$$

This factorization of the cross section is only possible for the quark-parton model, where no interaction occurs between the partons. Comparing equations 1.15 and 1.23 we obtain after integrating the δ function, the proton structure functions as being

$$F_1(x,Q^2) = \frac{1}{2}\sum_i e_i^2 f_i(x,Q^2) \tag{1.24}$$

$$F_2(x,Q^2) = \sum_i e_i^2 x f_i(x,Q^2) \tag{1.25}$$

which expresses the structure functions as the weighted sums of the density of all quark i, carrying a fractional momentum x. From the last two equations, we get

$$F_2(x,Q^2) = 2xF_1(x,Q^2) \Rightarrow F_L(x,Q^2) = 0 \Rightarrow \sigma_L = 0 \tag{1.26}$$

which is known as the Callan-Gross relation [8]. Moreover in the quark-parton model, the longitudinal photon cross section vanishes, which means, as the photon is strongly virtual that the partons do not carry any transverse momentum.

However, from the structure functions which are measured experimentally, one can estimate the quark momentum distribution functions and quantify the momentum carried by spin 1/2 partons in the proton. Combining the results from different experiments one finds [9]

$$\sum_q \int_0^1 dx x(q(x) + \overline{q}(x)) = 0.45 \tag{1.27}$$

where $q + \bar{q} = f_i$ for all the different quark and antiquark flavors. This fact (i.e. the right-hand-side is not equal to one) suggests that there are not only spin-1/2 partons in the proton, as only a fraction of the momentum (45%) is carried by them. In the following, we will see, that the remaining proton momentum is carried by the gluons, which are the bosons of the color interactions between the quarks, and which are neglected in the QPM.

1.4 Structure Functions in QCD

In the QPM, the proton contains only spin-1/2 non-interacting partons, the quarks. In QCD, the quarks can have three different "colors" (a more complex type of charge than in Quantum Electrodynamics) and are interacting by exchanging non-abelian gauge bosons called gluons. The strength of the interaction is determined by the strong coupling constant α_s, in a similar way as the coupling constant α in QED, but unlike α in QED, α_s decreases with increasing Q^2. This means that the strong interaction gets "weaker", the smaller the distance in between quarks, leading to "asymptotic freedom" for sufficiently high Q^2. Contrarily to the photon, which is electrically neutral, the gluon by itself carries color which arises from the non-abelian structure of the color field and therefore interacts with other gluons. The inclusion of gluons in calculating the structure functions is described in this section, from which the evolution equations are derived.

1.4.1 *ep*-Interactions at the Order α_s

Figure 1.2 shows the main diagrams which have to be taken into account for the cross-section calculation of the DIS process up to the first order in α_S. The diagram in figure 1.2*a* corresponds to the Born diagram. Taking into account the interactions

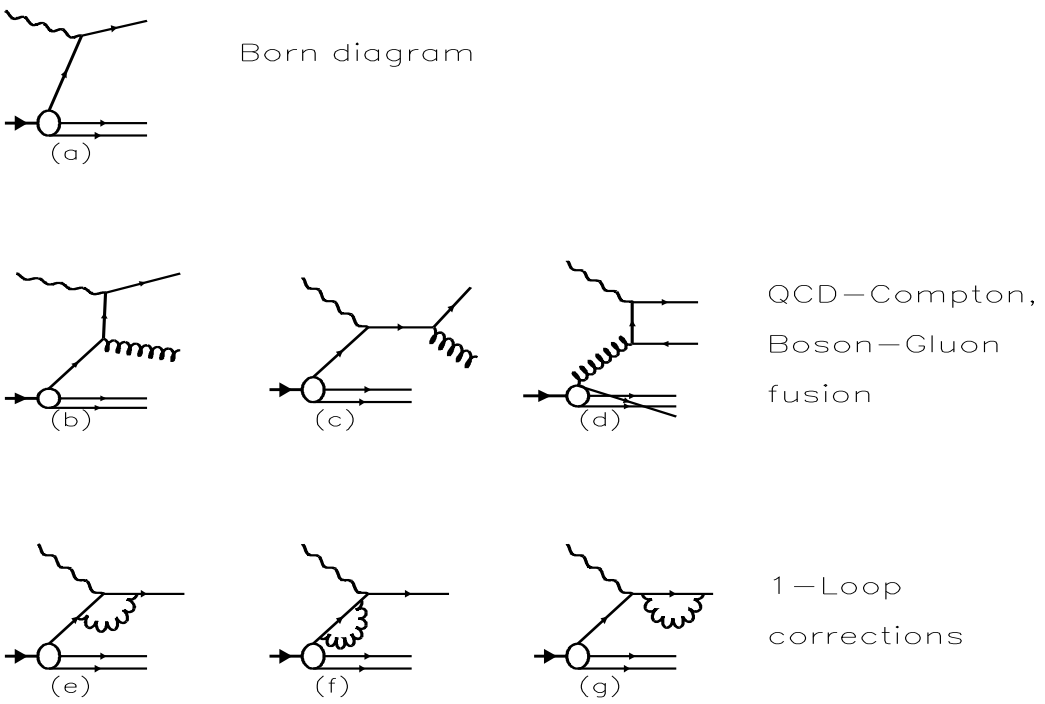

Figure 1.2: *Different processes up to the first order in α_s contributing to the matrix element calculation.*

at the first order of α_s, we have to consider the diagrams 1.2 $b-g$. The diagrams 1.2 b, c correspond to the QCD-Compton processes, where a gluon is radiated before or after the interaction with the photon, where as the diagram 1.2 d shows the interaction via photon gluon fusion. In figure 1.2 $e-g$, the virtual 1-loop corrections are pictured, which have to be taken into account in the cross-section calculation.

From equation 1.13, and using the definition of the longitudinal structure function given in equation 1.20, the structure functions F_2 and F_L can be expressed as function of the hadronic tensor $W_{\mu\nu}$ as

$$\begin{aligned} \frac{F_2(x,Q^2)}{x} &= \left(-g^{\mu\nu} + 3Q^2\frac{p^\mu p^\nu}{(p.q)^2}\right) W_{\mu\nu} \\ \frac{F_L(x,Q^2)}{x} &= -2Q^2\frac{p^\mu p^\nu}{(p.q)^2} W_{\mu\nu} \end{aligned} \tag{1.28}$$

Equation 1.12 can be written in momentum space and for the electron quark scattering where a struck quark carries the momentum fraction ω of the proton, as

$$\widetilde{W}_{\mu\nu}(\omega) = \frac{2\pi^3}{4\omega M}\sum_n \int \prod_{i=1}^{n}[\frac{d^3p_i}{(2\pi)^3 2p_{i0}}] < \omega p|J_\mu^\dagger(0)|n >< n|J_\nu(0)|\omega p > \delta^4(p_n - \omega p - q) \tag{1.29}$$

The tilde over $W_{\mu\nu}$ differentiates the partonic tensor from the hadronic tensor. Here the phase space is for n-final state particles, the δ function expresses the 4-momentum conservation at the vertex and the matrix elements describe the transition amplitude from the initial parton p carrying the momentum fraction ω to n final partons.

First we consider the QCD-Compton process $\gamma^*(q) + q(\omega p) \to q(p') + g(k)$ (figure 1.2 b, c) for its contribution to F_2. For this process in which we have two final state particles, d(PS) is given by the phase space along with the δ function

$$d(PS) = \frac{d^3p'}{(2\pi)^3 2p_0'}\frac{d^3k}{(2\pi)^3 2k_0}\delta^4(p' + k - \omega p - q) \tag{1.30}$$

The matrix elements are calculated using the Feynman rules for figure 1.2 b, c. We introduce the Lorenz invariant quantities for partons as

$$\hat{s} = (p+q)^2, \qquad \hat{t} = (p'-q)^2, \qquad \hat{u} = (p'-p)^2. \tag{1.31}$$

Integrating out the delta function and the azimuthal angle, the phase space reduces to just one single variable $\hat{t}$. After some calculations using the equations 1.28 and 1.29, the contribution to F_2 from the QCD-Compton process terms of invariant variables $\hat{s}$, $\hat{t}$ and $\hat{u}$ is found to be

$$\frac{\widetilde{F}_2^{q,r}(\omega)}{x} = \frac{2\alpha_s}{3\pi}\int_0^{t_{max}} \frac{d\hat{t}}{\hat{s}+Q^2}\left(-\frac{\hat{t}}{\hat{s}} - \frac{\hat{s}}{\hat{t}} + \frac{2\hat{u}Q^2}{\hat{s}\hat{t}} - \frac{6x^2}{\omega^2}\frac{\hat{u}}{Q^2}\right) \tag{1.32}$$

In this expression tilde means the partonic F_2, the superscript q indicates the quark-photon interaction and r the radiation of real gluon before or after the interaction

with the photon. The lower limit of the integration is zero and the integral is diverging at this limit. This arises because we have given the real gluon a zero mass. Associating a non zero mass m to gluon prevents the divergence and we can absorb this mass in the definition of the bare quark momentum distribution in the end of our calculations. This way of renormalization is known as the gluon mass regularization (MG) scheme, though there exist other schemes like the dimensional regularization scheme (DR) [9].

To get the proton structure function F_2, we must convolute the partonic $\widetilde{F}_2$ structure functions as

$$\frac{F_2(x,Q^2)}{x} = \sum_q e_q^2 \int d\omega q(\omega) \frac{\widetilde{F}_2(\omega)}{\omega} \tag{1.33}$$

By introducing $z = \frac{x}{\omega}$ and integrating over $\hat{t}$, we get

$$\frac{F_2^{q,r}}{x} = \sum_q e_q^2 \int_x^1 \frac{dz}{z} q\left(\frac{x}{z}\right) \left[\frac{\alpha_s}{2\pi}\left\{\frac{4}{3}\frac{1+z^2}{1-z}\log\left(\frac{Q^2}{m^2}\right)\right\} + \frac{2\alpha_s}{3\pi}\left\{\frac{1+z^2}{1-z}\log(1-z) + \frac{1+z^2}{1-z}(-2\log(z)) - \frac{3}{2}\frac{1}{1-z} + 4z + 1 + \frac{5}{4}\delta(1-z)\right\}\right] \tag{1.34}$$

In this equation the integral is independent from the regularization scheme, whereas the multiplicative term of $\frac{2\alpha_s}{3\pi}$ is only a function of z and depends on the regularization scheme, besides its process dependence. In order to distinguish among the different schemes and different processes, we put subscripts and superscripts, and call this term for the case of the gluon radiation $f_{F_2,MG}^{q,r}$. The coefficient function $\frac{4}{3}\frac{1+z^2}{1-z}$ of $\log(\frac{Q^2}{m^2})$ however is independent of any scheme of regularization and is a universal function that appears whenever a quark radiates a gluon. We call it the splitting function and denote it as $P_{qq}^r(z)$, where the superscript r specifies the real gluon emission contribution, and represents the probability of finding a quark q, which reduced its momentum fraction x by the fraction z after the emission of a gluon (figure 1.3 a). We note the singularities at $z = 1$, the upper limit of integration, for both $P_{qq}^r(z)$ and $f_{F_2,MG}^{q,r}$, however these singularities will cancel by the inclusion of the virtual gluon emission contributions $P_{qq}^v(z)$ and $f_{F_2,MG}^{q,v}$ (figures 1.2 e, f, g) as we will see in following. So the real gluon emission from the quark adds to F_2 as,

$$\frac{F_2^{q,r}}{x} = \sum_q e_q^2 \int_x^1 \frac{dz}{z} q\left(\frac{x}{z}\right) \left(\frac{\alpha_s}{2\pi} P_{qq}^r(z) \log\left(\frac{Q^2}{m^2}\right) + \alpha_s f_{F_2,MG}^{q,r}\right) \tag{1.35}$$

If we calculate the virtual gluon contribution (figures 1.2 e, f, g), we get the following expression for the radiative (r) and the loop (v) contribution,

$$\begin{aligned} \frac{F_2^q}{x} &= \frac{F_2^{q,r}}{x} + \frac{F_2^{q,v}}{x} \\ &= \sum_q e_q^2 \int_x^1 \frac{dz}{z} q\left(\frac{x}{z}\right) \left(\frac{\alpha_s}{2\pi}\left[\left\{\frac{4}{3}\frac{1+z^2}{1-z} + (2 + \frac{8}{3}\log(\epsilon))\delta(1-z)\right\}\log(\frac{Q^2}{m^2})\right]\right. \end{aligned}$$

$$+ \quad \frac{2\alpha_s}{3\pi}\left[\left\{\frac{1+z^2}{1-z}\log(1-z)+\frac{1}{2}\log^2(\epsilon)\delta(1-z)\right\}+\frac{1+z^2}{1-z}(-2\log(z))\right.$$
$$\left. - \quad \frac{3}{2}\left\{\frac{1}{1-z}-\log(\epsilon)\delta(1-z)\right\}+4z+1-\left(\frac{2\pi^2}{3}+\frac{5}{4}\delta(1-z)\right)\right]\Bigg) \tag{1.36}$$

By looking at this expression, one finds that each singular term in braces has its counterpart, such that the integration over these individual sums vanishes. If we write the above equation in terms of P and f, the expression becomes

$$\frac{F_2^q}{x} = \sum_q e_q^2 \int_x^1 \frac{dz}{z} q\left(\frac{x}{z}\right)\left(\frac{\alpha_s}{2\pi}P_{qq}(z)\log(\frac{Q^2}{m^2})+\alpha_s f^q_{F_2,MG}\right) \tag{1.37}$$

with

$$P_{qq}(z) = \left(\frac{4}{3}\frac{1+z^2}{1-z}\right)_+ \tag{1.38}$$

$$\alpha_s f^q_{F_2,MG} = \frac{2\alpha_s}{3\pi}\left\{(1+z^2)\left(\frac{\log(1-z)}{1-z}\right)_+ + \frac{1+z^2}{1-z}(-2\log(z))\right.$$
$$\left. -\frac{3}{2}\frac{1}{(1-z)_+}+4z+1+\frac{2\pi^2}{3}+\frac{5}{4}\delta(1-z)\right\} \tag{1.39}$$

The subscript + indicates that the corresponding functions are defined such that they do not contain the singularities and their integrals are always 0.

Finally the contribution from the photon-gluon fusion diagram 1.2 d is given by

$$\frac{F_2^g(x,Q^2)}{x} = 2\sum_q e_q^2 \int_0^1 \frac{d\omega}{\omega}\left\{\frac{\alpha_s}{2\pi}P_{qg}(z)\log\left(\frac{Q^2}{m^2}\right)+\alpha_s f^g_{F_2}(z)\right\} \tag{1.40}$$

Where the splitting function $P_{qg} = \frac{1}{2}(z^2+(1-z)^2)$ corresponds to the annihilation of a gluon into a quark-antiquark pair (figure 1.3 c), and the function f is

$$\alpha_s f^g_{F_2,MG}(z) = \frac{\alpha_s}{2\pi}\left\{-2P_{qg}(z)\log(z)-1+3z-3z^2\right\} \tag{1.41}$$

Four splitting functions can be defined, as pictured in figure 1.3 The two splitting functions, corresponding to the diagrams b and d of figure 1.3, can be computed in a similar way and have the following expressions:

$$\begin{aligned} P_{gq}(z) &= \frac{4}{3}\frac{1+(1-z)^2}{z} \\ P_{gg}(z) &= 6\left[\frac{z}{(1-z)_+}+\frac{1-z}{z}+\frac{11-\frac{2}{3}n_f}{12}\delta(1-z)\right] \end{aligned} \tag{1.42}$$

where n_f is the number of the flavors, which must be considered for the evaluation of the triple gluon vertex for the P_{gg} splitting function. The P_{gq} splitting function corresponds to a quark emitted by a quark transforming to a gluon.

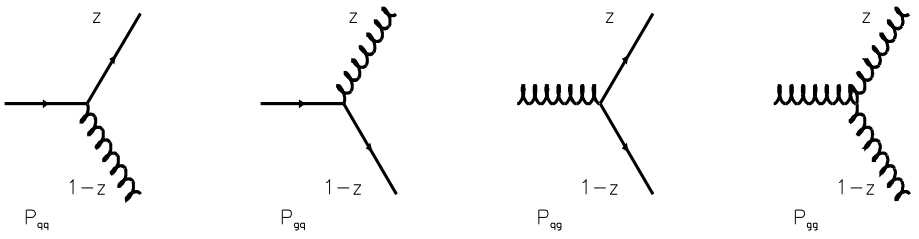

Figure 1.3: *Different processes corresponding to the four splitting functions.*

The structure function F_2 up to the order α_s is obtained by adding F_2^i from all the diagrams of the figure 1.2. Thus by adding equations 1.25, 1.37 and 1.40 we obtain the following expression for F_2,

$$\begin{aligned}\frac{F_2(x,Q^2)}{x} &= \frac{F_2^{born}(x,Q^2)}{x} + \frac{F_2^q(x,Q^2)}{x} + \frac{F_2^g(x,Q^2)}{x} \\ &= \sum e_q^2 \int_x^1 \frac{dz}{z}\left(q\left(\frac{x}{z}\right)+\overline{q}\left(\frac{x}{z}\right)\right)\left[\delta(1-z)+\frac{\alpha_s}{2\pi}P_{qq}(z)\log\left(\frac{Q^2}{m^2}\right)+\alpha_s f^q_{MG,F_2}(z)\right] \\ &\quad +2\sum e_q^2 \int_0^1 \frac{dz}{z} g\left(\frac{x}{z}\right) x\left[\frac{\alpha_s}{2\pi}P_{qg}(z)\log\left(\frac{Q^2}{m^2}\right)+\alpha_s f^g_{MG,F_2}(z)\right] \qquad (1.43)\end{aligned}$$

Here g is the gluon density of the proton. In a similar way, the longitudinal structure function F_L is

$$\begin{aligned}F_L(x,Q^2) &= \frac{F_L^{born}(x,Q^2)}{x} + \frac{F_L^q(x,Q^2)}{x} + \frac{F_L^g(x,Q^2)}{x} \\ &= \sum_q e_q^2 \int_x^1 \frac{dz}{z^3}\left(q\left(\frac{x}{z}\right)+\overline{q}\left(\frac{x}{z}\right)\right)\left[\alpha_s f^q_{F_L,MG}(z)+\alpha_s f^g_{F_L,MG}(z)\right] \qquad (1.44)\end{aligned}$$

where the f functions are

$$\begin{aligned}\alpha_s f^q_{F_L,MG}(z) &= \frac{2\alpha_s}{3\pi}2z \\ \alpha_s f^g_{F_L,MG}(z) &= \frac{\alpha_s}{2\pi}2z(1-z) \qquad (1.45)\end{aligned}$$

The new Q^2 dependent quark distribution functions can be extracted from F_2 using the relation

$$F_2(Q^2,x) = \sum_q e_q^2\left(q(x,Q^2)+\overline{q}(x,Q^2)\right) \qquad (1.46)$$

resulting in a integro-differential equation.

1.4.2 The DGLAP Evolution Equations

Although we cannot solve equation 1.46 for F_2 we can control the evolution of the parton distribution functions with respect of $\log(Q^2)$ with the help of the equation 1.43. The evolutions of the quark and gluon distribution function are more conveniently put in the double integro-differential equations, called the DGLAP equations after Dokshitzer, Gribov, Lipatov, Altarelli and Parisi [10] and are obtained from equations 1.43 and 1.46

$$\frac{\partial q(x,Q^2)}{\partial(\log Q^2)} = \frac{\alpha_s}{2\pi}(P_{qq} \otimes q + P_{qg} \otimes g) \tag{1.47}$$

$$\frac{\partial g(x,Q^2)}{\partial(\log Q^2)} = \frac{\alpha_s}{2\pi}(P_{gq} \otimes q + P_{gg} \otimes g) \tag{1.48}$$

Here $\otimes$ is defined as

$$P \otimes q = \int_x^1 \frac{dz}{z} P\left(\frac{x}{z}\right) q(z,Q^2) \tag{1.49}$$

Equations 1.47 and 1.48 can be described by diagrams *a* and *b* of figure 1.4 respectively. In a simplified way, we may say that

- the evolution of the quark density with Q^2 depends on the quark density before the emission of a gluon and the gluon density before creating a quark anti-quark pair
- the variation of the gluon density is coupled to the quark density before gluon emission and the gluon density at the triple gluon vertex itself.

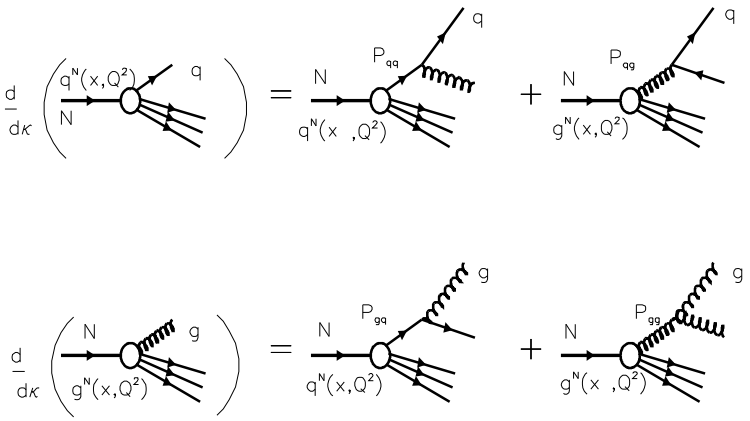

Figure 1.4: *DGLAP equations in leading order stating the rate of change of the quark and gluon distributions with respect to* κ *where* $\kappa = \frac{2}{11-\frac{2}{3}n_f}\log(\alpha(Q_o^2)/\alpha(Q^2))$.

1.4.3 The Leading-Log Approximation

The radiation of a single gluon is not the only process which contributes to the cross-section, multiple gluon radiation as pictured in figure 1.5, must also be considered. In order to compute these contribution we can use a perturbative development. In perturbative QCD, the processes are factorized in short-range phenomena, with

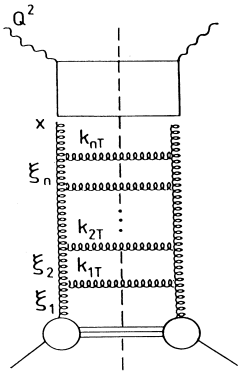

Figure 1.5: *Ladder diagram for multiple gluon radiation.*

$Q^2 > \mu^2_{fac}$, and long-range phenomena, $Q^2 < \mu^2_{fac}$. μ^2_{fac} is called the factorization scale and is chosen such as $\alpha_s(\mu^2_{fac})$ is sufficiently small to allow a perturbative development of the short-range processes.

Within this framework, F_2 can be expressed as a function of the parton densities as

$$F_2(x,Q^2) = \sum_{i=q,g} \int_0^1 d\xi C_i\left(\frac{x}{\xi}, \frac{Q^2}{\mu^2_{ren}}, \mu^2_{fac}, \alpha_s\right) q_i(\xi, \mu^2_{ren}, \mu^2_{fac}, \alpha_s) \tag{1.50}$$

where we sum over the quark and the gluon densities. The equation depends on two scales: the renormalization scale, which prevents ultraviolet divergences in which the momentum of virtual particles in 1-loop contributions gets infinite (similar to the mass regularization in section 1.4.1 and the factorization scale μ^2_{fac}, which defines the separation into short-range and long-range contribution. In the case of the gluon ladder, gluons emitted with $k^2_T > \mu^2_{fac}$ will contribute in the coefficient function and be computed in the perturbative development, whereas gluons emitted at $k^2_T < \mu^2_{fac}$ can not be computed perturbatively and contribute to the parton densities. Due to the factorization scale, the coefficient functions are infra-red stable, which means they will not contain singularities from gluons emitted collinearly.

In order to compute the coefficient functions, only the gluon ladders, being the dominant processes are included. The emitted gluons are supposed to be ordered in longitudinal momentum

$$\xi_1 > \xi_2 > \xi_3 > ..... > \xi_n > x \tag{1.51}$$

and strongly ordered in transverse momentum

$$Q^2 >> k^2_{nT} >> ... >> k^2_{2T} >> k^2_{1T} \tag{1.52}$$

In the leading-log approximation (LLA), only the dominating terms contributing as ${\alpha_s}^n(\log\frac{Q^2}{\Lambda^2})^n$ are considered. This is valid as long as

$$\alpha_s(k_{1T}^2)\log\left(\frac{Q^2}{k_T^2}\right) \sim 1 \tag{1.53}$$

$$\alpha_s(k_{1T}^2)\log\left(\frac{1}{x}\right) \ll 1 \tag{1.54}$$

In NLO, also the terms in $\alpha^{n+1}(\log\frac{Q^2}{\Lambda^2})^n$ are considered.

1.4.4 The Small-x Behaviour

At low x, the evolution of F_2 is driven by the gluon density and the evolution of the gluon density itself is dominated by the contribution from the triple gluon vertex, which leads to the approximation

$$\frac{dg(x,Q^2)}{d\log Q^2} \simeq \frac{\alpha_S}{2\pi}P_{gg}\otimes g \qquad \text{with} \qquad P_{gg}(z) \simeq \frac{6}{z} \tag{1.55}$$

After the derivation with respect to $\log 1/x$, this equation can be rewritten as

$$\frac{\partial^2(xg(x,Q^2)}{\partial\log 1/x\partial\log(\log(Q^2/Q_0^2)} = \frac{12}{\beta_0}xg(x,Q^2) \tag{1.56}$$

and can be solved exactly, leading to a double logarithmic scaling of the gluon density, as

$$xg(x,Q^2) \propto exp\sqrt{\frac{48}{\beta_0}\log\frac{1}{x}\log\left(\log\frac{Q^2}{Q_0^2}\right)} \tag{1.57}$$

The BFKL Equation

The leading log approximation is only valid under the assumption that

$$\alpha_s(Q^2)\log(1/x) \ll 1 \tag{1.58}$$

This condition is not fulfilled when x is becoming very small.
Therefore as $\alpha_s(Q^2)\log(1/x) \sim 1$, the BFKL equations (Balitski, Fadin, Kuraev and Lipatov) were proposed [11], where all the terms in $(\alpha_s\log(\frac{1}{x}))^n$ are summed. This approach needs strong ordering in x, i.e.,

$$x << x_n << ..... << x_2 << x_1 << x_0 \tag{1.59}$$

and weak ordering in transverse momenta

$$Q^2 \geq k_T^2 \geq k_{nT}^2 \geq ... \geq k_{2T}^2 \geq k_{1T}^2 \geq Q_0^2. \tag{1.60}$$

As at low Q^2 the behaviour of the gluon is dominating the behaviour of F_2, the BFKL equation is describing the evolution of the gluon density with $\log(1/x)$, using the function f defined by the derivated gluon density

$$f(x,k^2) = \left.\frac{d(xg(x,Q^2)}{\log Q^2}\right|_{k^2=Q^2} \tag{1.61}$$

and the evolution with $\log(1/x)$ is given by

$$\frac{\partial f(x,k^2)}{\partial \log 1/x} = \frac{\partial f_0(x,k^2)}{\partial \log 1/x} + \frac{3\alpha_S}{\pi}k^2 \int dk'^2 K(k^2,k'^2) f(x,k') \tag{1.62}$$

where f_0 is a non-perturbative term describing the coupling of the gluon to the proton and K the kernel.

From the BFKL equations, the strong rise of F_2 with decreasing x can be derived by an approximative solution of this equation [12], leading to a divergent gluon density:

$$xg(x,Q^2) \propto x^{-\lambda} \qquad \text{with} \qquad \lambda = \frac{3\alpha_S}{\pi} 4\log(2) \sim 0.5 \qquad \text{at} \qquad \alpha_S = 0.2 \tag{1.63}$$

However recent calculation at the NLO [13] have given large corrections reducing the amount of gluons at low x, which are still under theoretical debate (see for example [14]).

In order to relate the behaviour of the gluon density to F_2, the k_T factorization theorem was developed [15], which can be pictured as seen in figure 1.6.

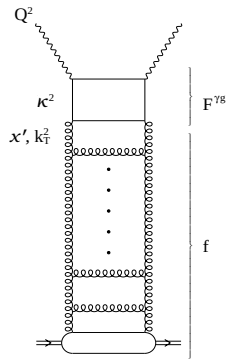

Figure 1.6: *Ladder diagram for multiple gluon radiation, indicating the k_T factorization.*

Within this framework, F_2 can be expressed as:

$$F_2 = F^{\gamma p} \otimes f + F^{np} \simeq \mathcal{C}(Q^2) x^{-\lambda_L} + F^{np} \tag{1.64}$$

where $F^{\gamma p}$ is the characterized by the photon-gluon fusion process convoluted to the derivated gluon density, $F^{np} \sim 0.4$ is a constant non-perturbative contribution

at $x \leq 0.05$ and determined from the F_2 behaviour at $x \sim 0.1$ [16]. However, predictions on F_2, from the BFKL inspired models, show a similar behaviour than in the NLO-DGLAP formalism, whereas the prediction on F_L are about a factor of two lower.

1.5 QCD Fits and Parton Distributions

Equations 1.47 and 1.48 do not predict the parton distribution functions at some arbitrary Q^2, but for a given distribution functions at some initial Q_0^2 scale, the DGLAP equations evolve them to an arbitrary scale. QCD fits aim at extracting the parton densities of the proton and the value of α_s. They are derived from the measured F_2 values, and may also take into account other processes in which the parton densities intervene, for example the prompt photon production $pp \rightarrow \gamma X$, which depends on the gluon density at high x or the Drell-Yann production $pp \rightarrow l^+l^-X$, which is sensitive to the sea quark densities. The result of these fits allows to test pQCD and to predict the cross-sections in yet unmeasured kinematic regions. In order to perform a QCD fit, first the parton densities are parameterized as functions of x. They are then injected in the DGLAP equations (eqs 1.47 and 1.48) at a given value of Q_0^2 and evolved according to these equations in Q^2. The splitting functions P and the coefficient functions C have been computed to NLO. The theoretical F_2 computed from the parton densities, is then adjusted to the data, taking into account the constraints from the quark counting rule on the valance quark densities u_v and d_v

$$\int_0^1 u_v(x,Q^2)dx = \int_0^1 u(x,Q^2) - 2\bar{u}(x,Q^2)dx = 2 \tag{1.65}$$

$$\int_0^1 d_v(x,Q^2)dx = \int_0^1 d(x,Q^2) - 2\bar{d}(x,Q^2)dx = 1 \tag{1.66}$$

and from the momentum sum rule

$$\int_0^1 x(u_v + d_v + g + 2(u_s + d_s + s_s + c_s + b_s))dx = 1 \tag{1.67}$$

where the subscript s indicates the contribution from the sea-quarks. Various groups have performed QCD fits, differing in the chosen input data, the type of parton density parametrization and additional assumptions on parton densities. In the following, two of them are described in more detail.

1.5.1 The MRST Parametrization

In this parametrization due to Martin, Robert, Stirling and Thorne [17], the parton distribution functions are parameterized at a scale $Q_0^2 = 1GeV^2$ as

$$xu_v(x) = a_u x^{\alpha_u}(1-x)^{\beta_u}(1 + b_u\sqrt{x} + c_u x) \tag{1.68}$$

$$xd_v(x) = a_d x^{\alpha_d}(1-x)^{\beta_d}(1 + b_d\sqrt{x} + c_d x) \tag{1.69}$$

$$xS(x) = a_s x^{\alpha_s}(1-x)^{\beta_s}(1 + b_s\sqrt{x} + c_s x) \tag{1.70}$$

$$xg(x) = a_g x^{\alpha_g}(1-x)^{\beta_g}(1+c_g x) \tag{1.71}$$

with 3 active flavors u, d and s. S stands for the total sea quark density. The constraints put on the light sea quarks at $Q^2 = Q_0^2$ are

$$2\bar{u} = 0.4S - \Delta \tag{1.72}$$

$$2\bar{d} = 0.4S + \Delta \tag{1.73}$$

$$2\bar{s} = 0.2S \tag{1.74}$$

which means that the u and d quarks densities contributing t o the sea can be different by Δ and the strange contribution to the sea accounts for 20%. The c and b contributions are only generated above their threshold $Q^2 > m_q^2$ from boson-gluon fusion.

To obtain the parameters of the parton distribution functions, large amount of data points from different experiments i.e. H1, ZEUS, HERMES, BCDMS, NMC, E665 and SLAC was used to cover the maximum possible kinematic region. It was further required to satisfy the neutrino data constraints by comparing with the structure functions $F_2^{\nu n}$ and $xF_3^{\nu n}$ as measured by the CCFR experiment [18]. The parameterized gluon distribution was constrained by the prompt-photon production from the E706 experiment at $x \geq 10^{-3}$. Contrarily to the former parametrization [19] where the light sea was weakly constrained by a single measurement of $\bar{u} - \bar{d}$ at $x = 0.18$ from NA51 [20], the present parametrization is strongly constrained by the Drell-Yann production in the range $0.03 \leq x \leq 0.35$ from the E866 experiment [21]. The CDF measurement of the asymmetry of the rapidity distribution of the charged lepton from $W^{\pm} \to l^{\pm}\nu$ provides a tight constraint on the light valence ratio u/d [22]. The new more precise measurements of $F_2^{\mu p}$, $F_2^{\mu d}$ and $F_2^{\mu d}/F_2^{\mu p}$ by NMC constrains further the parton densities [23]. Finally the parameterized charm quark distribution was required to satisfy the recently measured charm structure function at HERA [24].

1.5.2 The GRV Model

The GRV (Glück, Reya and Vogt) model [25] was developed as a dynamical ("radiative") parton model in order to account for the QCD evolution of the parton densities. This means that all parton densities even the gluons are assumed to have a valence like form at a very low Q^2 scale, typically $\mu^2 \approx 0.3\ GeV^2$. The sea quarks are then generated dynamically via boson-gluon fusion, and were predicted to rise strongly at low x [26, 27, 28] which was confirmed by the very first measurements at HERA. The parton densities are parameterized as following

$$xu_v(x) = a'_u x^{\alpha'_u}(1-x)^{\beta'_u}(1 + b'_u\sqrt{x} + c'_u x + d'_u x^{3/2}) \tag{1.75}$$

$$xd_v(x) = a'_d x^{\alpha'_d}(1-x)^{\beta'_d}(1 + b'_d\sqrt{x} + c'_d x + d'_d x^{3/2}) \tag{1.76}$$

$$x\Delta(x) = a'_\delta x^{\alpha'_\delta}(1-x)^{\beta'_\delta}(1 + b'_\delta x) \tag{1.77}$$

$$x(\overline{u}(x) + \overline{d}(x)) = ex^{\gamma}(1-x)^{\eta}(1+fx) \tag{1.78}$$

$$xg(x) = g' x^{\alpha'_g}(1-x)^{\beta'_g} \tag{1.79}$$

The GRV parametrization assumes the strange quark distribution $s(x) = \overline{s}(x) = 0$ at the initial scale leading to an SU(3) broken sea. The light quarks u, d and s, are supposed massless whereas the heavy quark masses used are

$$m_c = 1.4\ GeV \qquad m_b = 4.5\ GeV \qquad m_t = 175\ GeV \tag{1.80}$$

The remaining constraints are same as in MRST.

1.6 The Transition towards Photoproduction

In QCD, we generally distinguish two major types of interactions, "hard interactions", where we can determine a factorization scale, which is sufficiently important such that perturbative calculations can be performed, and "soft interactions", which can only be described by phenomenological models. In ep scattering, the most natural interaction scale is given by the exchanged photon: for DIS-events at Q^2 greater than a few GeV^2, perturbative calculations can be safely applied, whereas photoproduction processes at $Q^2 \simeq 0$ can be described by Regge theory, as used for example in the model of Donnachie-Landshoff [29], where F_2 is the sum of two Regge trajectories, which are motivated by the contributions of Reggeon exchange (particles carrying non-zero quantum numbers) and Pomeron exchange (particles carrying zero quantum numbers).

With the HERA data at low Q^2, the transition region between the two regimes can be studied explicitally and several approaches were developed in order to describe the behaviour of the cross-section over the full kinematic region. The two most successful models, the Badelek-Kwiechinski model and the ALLM-parametrization are described briefly.

1.6.1 The ALLM Parametrization

The ALLM parametrization (Abramowicz, Levin, Levy and Maor) [30] is the result of a fit on F_2 data from various experiments, photoproduction cross-sections, and the cross-sections from hadron-hadron interactions. The Regge theory inspired fit is based on the idea, that F_2 can be obtained from a Pomerons and a Reggeon contribution as

$$F_2(x,Q^2) = \frac{Q^2}{Q^2+m_0^2}\left(F_2^{I\!P}(x,Q^2) + F_2^{I\!R}(x,Q^2)\right) \tag{1.81}$$

with

$$\begin{aligned} F_2^{I\!P}(x,Q^2) &= c_P(t) x_P^{\alpha_P(t)}(1-x)^{b_P(t)} \\ F_2^{I\!R}(x,Q^2) &= c_R(t) x_P^{\alpha_R(t)}(1-x)^{b_R(t)} \end{aligned} \tag{1.82}$$

the scale t is defined as

$$t = \log\left(\frac{\log\frac{Q^2+Q_0^2}{\lambda}}{\log\frac{Q_0^2}{\lambda}}\right) \tag{1.83}$$

The t dependence of the coefficients c_P, c_R, b_P, b_R as well as $\alpha_P(t)$ and $\alpha_R(t)$ is expressed by two parameterized functions, such that this fit contains 23 free parameters, which allow to describe the cross-section measurements from fixed target and the HERA experiments in the whole phase space in x ($3 \cdot 10^{-6} \leq x \leq 0.85$) and Q^2 ($0\ GeV^2 \leq Q^2 \leq 5000\ GeV^2$).

1.6.2 The Badelek-Kwiechinski Model

In the Badelek-Kwiechinski Model (BK) [31], the structure function is composed of a non-perturbative part based on the Vector Meson Dominance Model (VDM) and a perturbative part based originally on the GRV approach, but which can be replaced by any type of NLO QCD parametrization:

$$F_2(x,Q^2) = F_2^{VDM}(x,Q^2) + \frac{Q^2}{Q^2+Q_0^2} F_2^{QCD}(x,Q^2) \tag{1.84}$$

In VDM, the photon is considered as a hadronic system, carrying the quantum numbers of a vector meson. $F_2^{VDM}(x,Q^2)$ contains therefore the contribution of the production cross-section of all light vector mesons, with $M_V^2 < Q_0^2$, Q_0^2 defining the limit between the VDM and the QCD regime and can be expressed as:

$$F_2(x,Q^2) = \frac{Q^2}{4\pi} \sum_V \frac{M_V^4 \sigma_V(W)}{\gamma_V^2 (Q^2+M_V^2)^2} \tag{1.85}$$

where σ_V is the total vector meson-nucleon cross-section and γ_V^2 the coupling constant of the photon to the vector meson. If only a finite number of vector meson is considered, the F_2^{VDM} contribution is vanishing at high Q^2. For $Q_0^2 \simeq 1.2\ GeV^2$ the considered vector mesons are according to their masses ρ, ω and ϕ. The extension of VDM, by taking into account the continuous contribution in the perturbative region of the phase space is called Generalized Vector Meson Dominance Model (GVDM).

1.7 Summary

We have introduced the formalism which relates the structure functions to the strong interaction theory QCD. Using the framework of perturbative theory, the evolution of the structure function can be predicted as a function of $\log(Q^2)$ by the DGLAP evolution equations, and current parametrizations of the parton densities obtained by NLO QCD fits have been presented. At small x, the gluon density is dominating the F_2 behaviour and can be predicted by the LL-approximation to have a double logarithmic scaling behaviour. This approximation however is only valid, if $\log(1/x)$ is small, whereas in the opposite case, the BFKL formalism was proposed. The constraints on the behaviour of F_2 from the DGLAP and the BFKL equations, are not important enough to discriminate them experimentally, and different observables as for example F_L will be necessary in the future in order to establish clearly the underlying dynamics. The transition from perturbative to non-perturbative QCD at very low Q^2 has been discussed in the form of two different models, either using

a Regge theory inspired Ansatz or a generalization of the Vector Meson Dominance Model. The results of the measurement presented in this thesis will be compared to the two approaches.

Bibliography

[1] E.D. Bloom et al., **Phys. Rev. Lett.** 23(1969) 930.

[2] M. Breidenbach et al., **Phys. Rev. Lett.** 23(1969) 935.

[3] R.P. Feynman, **Photon-Hadron Interactions**, Reading, MA, Benjamin (1972).

[4] F. Halzen, A.D. Martin, **Quarks and Leptons**, J.Wiley & Sons 1984.

[5] T.P. Cheng, L.F. Li, **Gauge theory of elementary particle physics**, Oxford 1984.

[6] R.G. Roberts, **The structure of the proton**, Cambridge 1990.

[7] J. Blümlein et al., **HERA Workshop, vol 1**, 1987.

[8] C.G. Callan and D. J. Gross, **Phys. Rev. Lett.** 22(1969) 156.

[9] R.D. Field, **Applications of Perturbative QCD** , Addison-Wesley 1989.

[10] V.N. Gribov and L.N. Lipatov, **Sov. J. Nucl. Phys.**15 (1972) 438;
L.N. Lipatov, **Sov. J. Nucl. Phys.**20 (1975) 96;
G. Altarelli and G. Parisi, **Nucl. Phys.**B126 (1977) 298.

[11] E.A. Kuraev, L.N. Lipatov and V.S. Fadin, **Sov. Phys JETP** 45 (1977) 199;
Y.Y. Balitsky and L.N. Lipatov, **Sov. J. Nucl. Phys.** 28 (1978) 822.

[12] J. Kwiecinski et al., RAL-90-053 (1990).

[13] V.S. Fadin and L.N. Lipatov, **Phys. Lett.** B429 (1998) 127.

[14] R. Thorne, **Preprint OUTP**-9902 (1999).

[15] S. Catani and F. Hautman, **Phys. Lett.** B315 (1993).

[16] J. Kwichinski, **Report 1620/PH**, IFJ Cracow (1993).

[17] A.D. Martin et al, **hep-ph/9803445**.

[18] CCFR collaboration, W.G. Seligman et al., **Phys. Rev. Lett.** 79 (1997) 1213.

[19] A.D. Martin et al, **Phys. Rev.** D50 (1994) 6734.

[20] NA51 collaboration, A. Baldit et al., **Phys. Lett.** B332 (1994) 244.

[21] E866 collaboration, E.A. Hawker et al., **hep-ex/980301**.

[22] CDF collaboration, A. Bodek at The Cracow International Symposium on Radiative Corrections (CRAD96), Cracow Poland May 1,1996 **Acta Phys. Polon.** B28 (1997) 477.

[23] NMC collaboration, M. Arneodo et al., **Nucl. Phys.** B483 (1997) 3.

[24] H1 collaboration, C. Adloff et al., **Z. Phys.** C72 (1996) 593;
ZEUS collaboration, J. Breitweg et al., **Phys. Lett.** B407 (1997) 402

[25] M. Glück, E.Reya, A. Vogt, **preprint DO**-TH 98/07.

[26] M. Glück, E.Reya, A. Vogt, **Z. Phys.** C53 (1992) 127.

[27] M. Glück, E.Reya, A. Vogt, **Phys. Lett.** B306 (1993) 391.

[28] M. Glück, E.Reya, A. Vogt, **Z. Phys.** C67 (1995)433.

[29] A. Donnachie and P.V. Landshoff, **Z. Phys.** C61 (1994) 139.

[30] H. Abramowicz et al., **Phys. Lett.** B269 (1991) 465;
H. Abramowicz and A. Levy, **DESY-Report** 97-251.

[31] B. Badelek and J. Kwiechinski, **Nucl. Phys.** B370 (1992) 278;
B. Badelek and J. Kwiechinski, **Phys. Lett.** B320 (1994) 50.

Chapter 2

The HERA Accelerator and the H1 Detector

The HERA collider (Hadron Electron Ring Accelerator) is producing electron-proton collisions for the H1 and ZEUS experiments with an electron beam energy of 27.6 GeV and a proton beam energy of 820 GeV, resulting in a center of mass energy $\sqrt{s} = 301$ GeV. H1 (and similarly ZEUS) is a nearly hermetic multi-purpose detector [1] (see figure 2.1) equipped from inside out with a tracking system, several calorimeters, a superconducting solenoid delivering a magnetic field of 1.2 T and dedicated

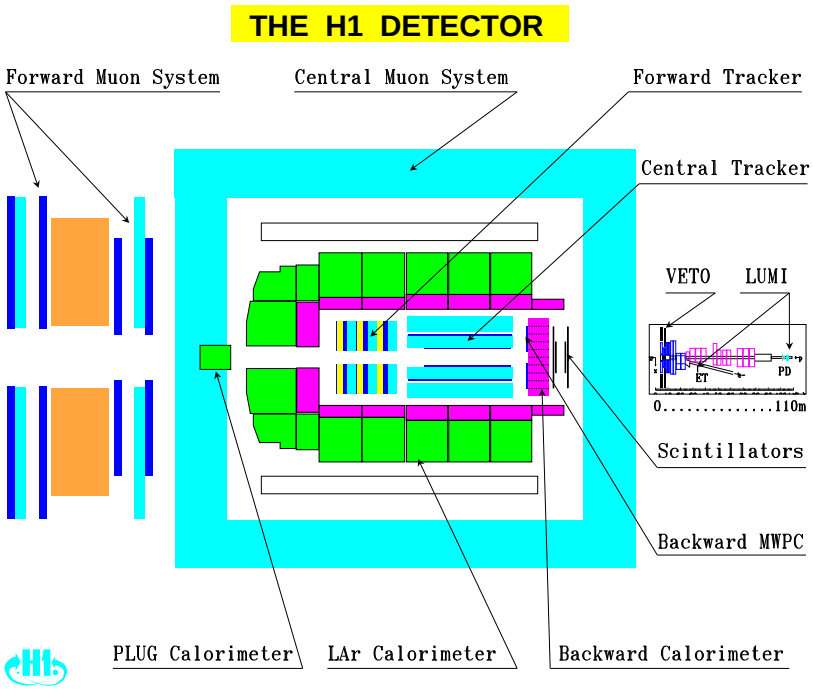

Figure 2.1: *Longitudinal view of the H1 Detector before the upgrade of the backward region.*

muon detectors. The detector is asymmetric, reflecting the asymmetry in the beam energies, with a small calorimeter in the backward region [1], dedicated mostly to the measurement of the scattered electron at low Q^2 and a denser forward region, where mainly the fragments of the proton are observed.

Since 1992 the luminosity increased roughly by a factor of 10 each year from 25 nb^{-1} in 1992 to 35 pb^{-1} in 1997. The accumulated luminosity allows for a precise study of the structure functions especially in the low x and low Q^2 region. In order to improve the precision of these measurements, an upgrade program of the rear part of the H1 detector was undertaken replacing the Backward Proportional Chamber (BPC) by a Backward Drift Chamber (BDC) and the Backward Electro-Magnetic Calorimeter (BEMC) by a 'Spaghetti' Calorimeter (SpaCal).

The present chapter describes briefly the HERA accelerator and the H1 detector. After introducing HERA in section 2.1, section 2.2 describes the luminosity system and the different methods used for the luminosity measurement. Section 2.3 discusses the tracker system and section 2.4 the calorimeter system with emphasis given to the new SpaCal calorimeter as the present analysis relies strongly on this detector. The other subdetectors are not used in this analysis and their description can be found in [1].

2.1 The HERA Accelerator

Before obtaining the final beam energies of 27.6 GeV for the electrons and of 820 GeV for the protons, different steps in pre-acceleration are taken [2], from the bunch formation to the final beam energies (see fig 2.2).

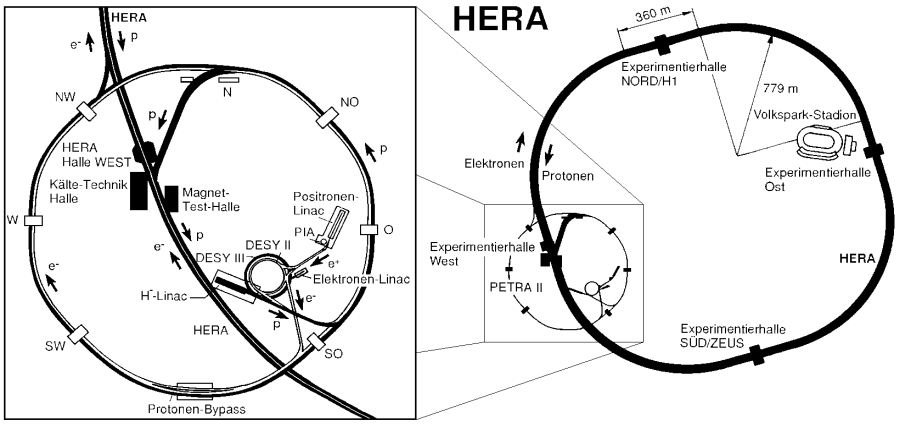

Figure 2.2: *The HERA accelerator with the location of the four experiments and an enlarged view of the preaccelerators.*

For the electrons, first a LINAC injects individual electrons of 500 MeV into a small storage ring which produces single bunches of $\sim$ 60 mA. These bunches

[1] The positive z axis is defined w.r.t the proton beam direction

are transferred to DESY II which accelerates them to 7 GeV. Then 70 bunches of 14 GeV are collected in PETRA. These bunches are finally transferred to the main storage ring HERA, where up to 210 bunches are circulating and accelerated to the nominal beam energy.

The protons pass through almost the same kind of processes before attaining the final energies. A different LINAC produces 50 MeV H^- ions, which are accumulated in DESY III. In DESY III, the charge exchange injection takes place within 10 turns of accumulation by stripping off the electrons of the H^- ions passing through a thin foil in order to obtain protons in individual 7.5 GeV bunches which are then transfered to PETRA and cumulated into 70 bunches each of 40 GeV. Finally they are transfered to HERA and accelerated to 820 GeV.

A bunch of whether electron or proton has a Gaussian distribution of particles both in the x- and y-directions [3]. Each bunch has a length of 7.8 mm for the electron beam and $110 - 150$ mm for the proton beam at their maximum energies, determinating the width of the interction vertex distribution in z. Their widths at the interaction points are 0.3 mm (for the electrons) and 0.32 mm (for the protons) while their heights at the interaction points are 0.04 mm and 0.1 mm respectively, leading to an ellipsoidal transverse cross-section. Each bunch contains about 3.5×10^{10} electrons and 10^{11} protons. The spacing between the bunches is 96 ns, leading to a collision frequency of 10.4 MHz Some bunches have no counterpart, called pilot bunches, and used to study beam induced backgrounds.

If we look at the bunch structure of the electrons (see fig 2.3), we see a main

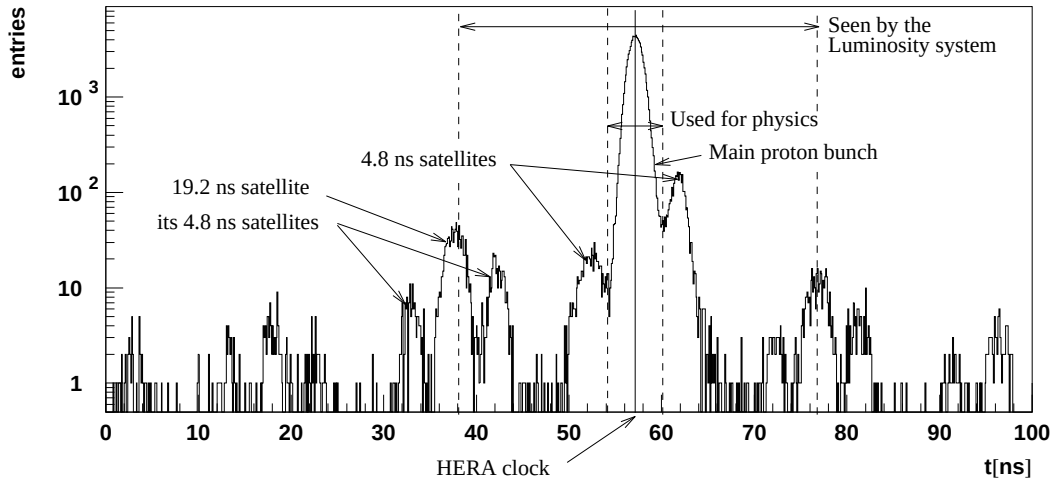

Figure 2.3: *Bunch structure of the electron beam with the main bunch and the satellite bunches. Indicated is the part seen by the luminosity system.*

peak and besides satellite bunches which are 4.8 ns later and -4.8 ns earlier, than the main bunch. The contribution of these satellite bunches are varying in time and between different fills. As the interactions from these bunches contribute to the luminosity measurements but are cut by the vertex requirement in the analysis, we

have to correct for their contribution in the luminosity determination. The mean correction factor is -3.6% for the 95 nominal vertex data.

The main running parameters for HERA in 1995 are summarized in table 2.1 and compared to the performance during the 1994 e^+ running. The performance of the machine improved, especially for the mean proton currents, which is partially related to an increase of the number of stored bunches, but also higher currents in each bunch could be achieved. The design values for HERA are also given.

	1995 e^+	1994 e^+	nominal
lepton energy (GeV)	27.6	27.6	30
proton energy (GeV)	820	820	820
$\langle I_e \rangle$ (mA)	18.4	17.0	60
$\langle I_p \rangle$ (mA)	54.0	41.0	160
number of bunches	174 (+21 pilots)	153 (+21 pilots)	210
peak luminosity $(cm^{-2}s^{-}1)$	6.0 10^{30}	4.3 10^{30}	1.5 10^{31}

Table 2.1: *Main parameters of HERA for the 1995 data taking compared to the 1994 e^+ running and the nominal values.*

The two interaction regions of the electron and the proton beam are equipped with the H1 detector in the north and with the ZEUS detector in the south. In the east hall, the HERMES detector is installed, where the electron beam is scattered on a gas target. The beam and the target are polarized for studies of polarized structure functions and semi-inclusive measurements on the hadronic final state. In the west hall, the HERA-B experiment uses the proton beam on wire targets and is aiming at observing direct CP violation in the $B\bar{B}$ system.

2.1.1 Kinematic Constraints for HERA-Events

From the HERA-beam energies, we can easily compute the accessible $x - Q^2$ domain for DIS events: the kinematic limit in Q^2 with the available center of mass energy is 90600 GeV^2, whereas at $Q^2 = 1\ GeV^2$ an x value of $1.1 \cdot 10^{-5}$ can be reached. Figure 2.4 shows the lines of constant energy and angle, for both the scattered electron (upper figure) and the "struck quark" in the naive QPM (lower figure) over this kinematic region. The region is delimited by a diagonal, corresponding to the kinematic constraint of $y < 1$. Lines of constant y will be parallel to this diagonal.

The relation between x, y and Q^2, implies that the lowest x values are obtained also at lowest Q^2 and at high y. The reach at low Q^2 is limited by the θ-acceptance of the scattered electron in the backward region: considering an acceptance limit due to the beam-pipe of 2^o, electrons of events with with $Q^2 < 0.1\ GeV^2$ are escaping the backward beam-pipe.

In order to reach low x values, we must be able to detect events at high y, which means at low electron energy. If electrons can be identified with energies down to 3 GeV, $y \sim 0.9$ can be reached, however this is far from being trivial, as the

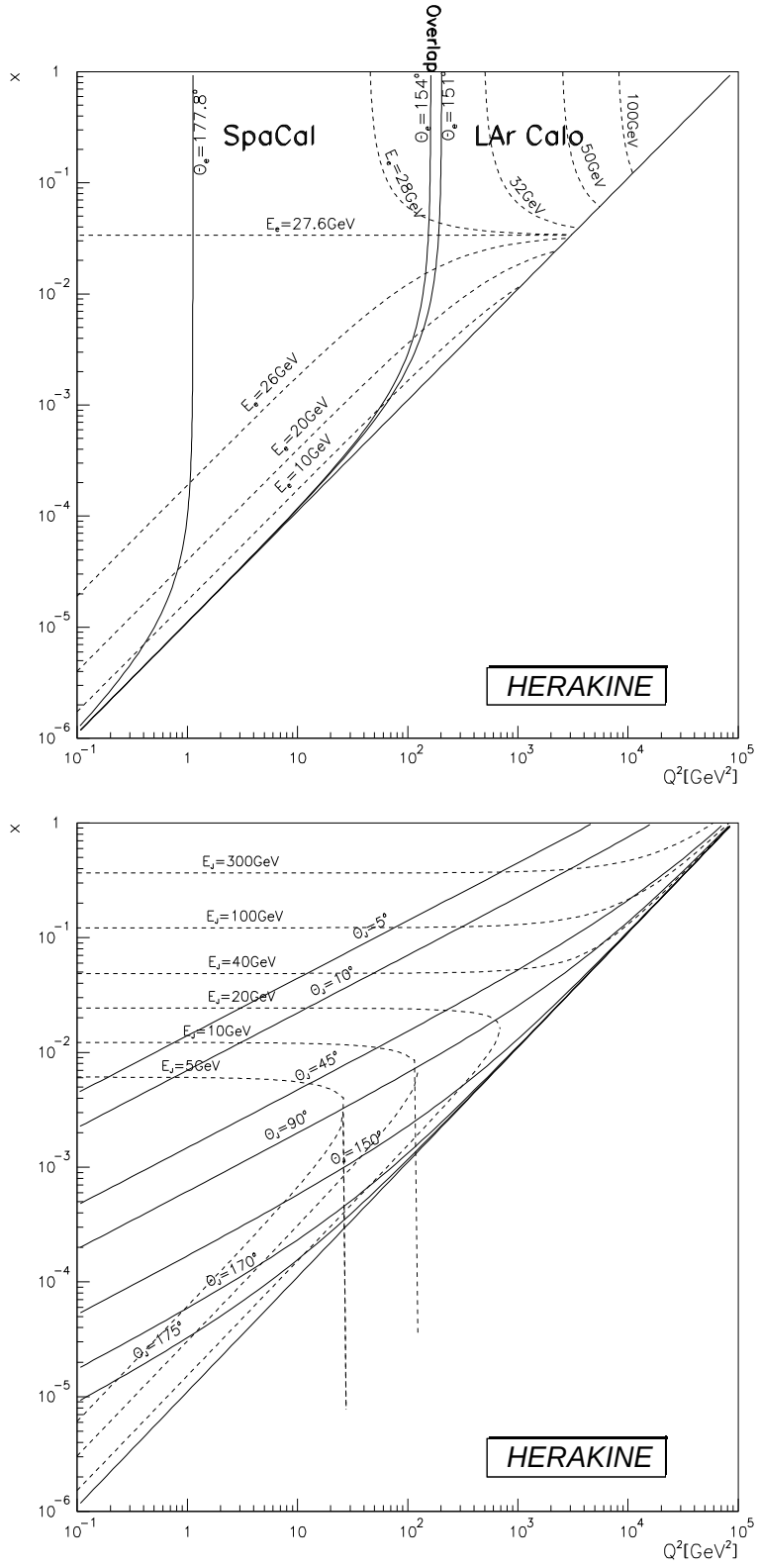

Figure 2.4: *Hera kinematics: x and Q^2 regions as function of the energy and the angle of the scattered electron, indicating the calorimeter in which it is detected (upper plot) and as function of the theoretic energy and angle of the struck quark in the QPM (lower plot).*

electron/pion separation is very difficult at low energy and therefore misidentification can easily occur. This effect is amplified, by the fact that at high y, the struck quark is backscattered, creating an low energetic jet in the backward region of the detector.

At high x, the detection of events is limited by the hadronic final state, which is directed more and more in the forward direction, as we are going towards lower y. The background conditions at HERA however impose the presence of an event vertex measured with the tracking chambers from either the electron or the hadronic final state, imposing therefore a limit on the measurable region towards high x. Besides, the wide range in x covered by a rather small variation in the electron energy, indicates that we must use the hadronic final state information in order to accurately reconstruct the event kinematics, as even small errors on the electron energy will induce huge migration in the $x - Q^2$ plane.

As the cross-section in DIS is varying as $1/Q^4$, we will get the majority of events at low Q^2, i.e. low electron scattering angles. Limiting the event rate, due to a limited amount of trigger band-width, is therefore be done by prescaling trigger for electron candidates in the very backward region.

2.2 The Luminosity System

For the luminosity determination, the cross-section of QED processes which can be computed precisely, are measured and from the comparison with the expected value the luminosity is extracted. At HERA, one can use essentially two methods for the luminosity determination [4]:

- Bethe-Heitler Bremsstrahlung: The Bethe-Heitler process $ep \to e\gamma p$ has a very large cross section of about 100 mb for the emission of a photon at low angles below 17 μrad. This allows for a measurement with a very high statistical precision, but at these angles, the electron and the photon are escaping the main detector and have to be detected in special calorimeters placed further away along the beam pipe.

- QED-Compton: In the elastic $ep \to ep\gamma$ or inelastic $ep \to eX\gamma$ QED Compton process, the scattered electron and photon angles are large and both can be clearly seen in the main detector. The small cross section $\sigma_{vis} \sim 10\ nb$ however, prevents a good statistical precision. This method is therefore only used for cross-checks [5].

The Luminosity Detector

The electron and photon of the Bethe-Heitler process are detected by the luminosity detector, which consists of an electron tagger and a photon detector (see figure 2.5), located upstream of the main H1 detector [6]. The main electron tagger (ET) for the luminosity system is a 49 channel crystal Cherenkov calorimeter with a cross section area of 15.4 $cm \times 15.4\ cm$ and a depth of 20 cm, located at $z = -33.4\ m$. Two additional new electron tagger ET44 and ET8, analogous to ET but with only

6 channels (2×3 crystals), are situated at $z = -44\ m$ and $z = -8\ m$. These taggers are not used for the luminosity measurement.

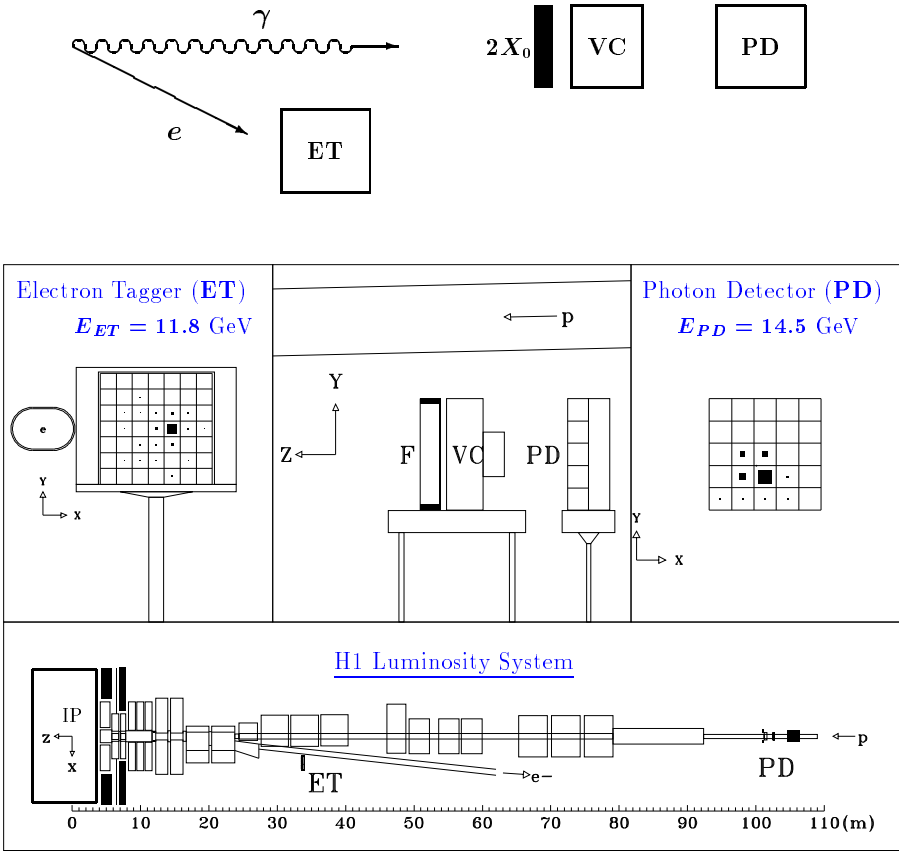

Figure 2.5: *Schematic view of the Luminosity System. Above is indicated the Bethe-Heitler process and the principle of its detection. In the middle, an event seen in the Electron Tagger and the Photon Detector is shown along with the setup of the Veto-Counter and the Photon Detector. Below, the magnets from the interaction point in the main detector to the luminosity detectors are indicated.*

A 25 channels crystal Cherenkov calorimeter with a cross sectional area of 10 $cm \times 10\ cm$ and a depth 20 cm is used as photon detector (PD) and located at $z = -103.1\ m$. A veto counter (VC), a water Cherenkov detector of 28 cm width, is just in front of the PD at $z = -102.8\ m$ and used as protection against the high synchrotron radiation flux.

The system has high radiation resistance with a good energy resolution of $\sigma_E/E = 15\%/\sqrt{E} \oplus 1\%$, a resolution in x and y of $\sigma_{x,y} = 0.3 - 1.2\ mm$ and a timing resolution below 3 ns for both ET and PD.

Other Functions of the Luminosity System

Besides the luminosity measurement, these detectors are used to monitor the behaviour of the electron beam. The ET is also used, together with the two additional taggers, to measure electrons in photoproduction events at $Q^2 \approx 0\ GeV^2$. In these events the angular deviation of the electron is so small that it escapes into the beam-pipe and may then be detected, within their acceptance, by these electron taggers. As these events are the main background at low energy in DIS, the tagged events are used for the background estimation in our event sample.

2.2.1 The Luminosity Determination

The luminosity[2] is obtained from the following formula [6]:

$$\mathcal{L} = \frac{N_{BH}^{ep}(E_\gamma > E_{min})}{\sigma_{BH}(E_\gamma > E_{min})} \tag{2.1}$$

As the system is very close to the beam pipe, there is a large contamination from synchrotron radiation, predominantly at low energies. This background can be avoided by putting a lower limit on the photon energy E_{min}. The choice of a reasonable E_{min} further reduces pile-up effects. The luminosity was corrected for limited geometrical acceptance of the detector and the trigger efficiencies. The number of Bethe-Heitler events N_{BH} are determined in H1 by two different methods.

- **Coincidence (γe) method:** This method uses only events, where the electron and the photon are detected in coincidence. It is very sensitive to small variations in the beam optics due to the limited acceptance of ET, as small changes in the vertical position of the electron beam, may make the electron escape the tagger. However the advantage is its stability against small variations in the trigger threshold. Moreover as one is measuring the energies of both the electron and the photon, a better relative energy calibrations is achieved. In figure 2.6, the correlation of the energy measured in the photon and in the electron detector is shown, where the sum of the two energies should be equal to the beam energy of the electron. In the 1995 data taking this method was used for the online analysis due to these two advantages.

- **Single photon (γ) method:** Here only the information obtained from the PD is used. Due to the larger acceptance of the PD compared to the ET, this method is less sensitive to variations in the beam optics. However, it is less stable against variations in the trigger threshold and a better energy calibration is needed as the relative calibration with the scattered electron is not available. Therefore this method is less adapted for the online analysis, and used for the precise offline determination of the luminosity.

[2] $\mathcal{L}$ denotes the total time-integrated luminosity (b^{-1}).

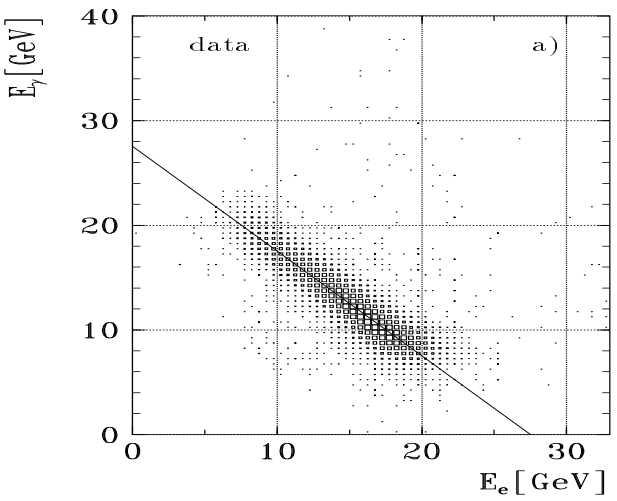

Figure 2.6: *Correlation between the photon energy measured in the photon detector and the electron energy in the electron tagger used for the energy calibration for luminosity system.*

Uncertainties on the Luminosity Measurement

The most important contributions to the uncertainties of the luminosity measurement are coming from the theoretical uncertainty on the calculated cross-section, σ_{BH}, which is 0.47% and from the photon energy calibration and the PD energy resolution, which leads equally to and uncertainty of 0.47 % at $E_{min} = 10\ GeV$. Pile-up effect occur with the emission of more than one BH photon in a single bunch crossing (BC), such that their energies are summed and wrongly estimated as the energy of a single photon. The error estimated from this effect is 0.11 %. The statistical errors from the electron gas background subtraction contribute 0.21% [6].

The total corrections on the on-line luminosity measurements determined from the off-line study are -2.7 ± 1.07 % for the nominal vertex data and -5.4 ± 1.14 % for the shifted vertex data. The satellite bunch corrections determined from the offline analysis for 91 % of the nominal vertex 1995 data (only 'Good' or 'Medium' runs) are -3.6 % with a systematic error of ± 0.4 % from FToF (Forward Time of Flight) measurements and $^{+1.6}_{-0.3}$ % from the limitation of the method used. The total error on the luminosity measurement is 1.97%.

2.3 The Tracking System

The H1 tracking system [7] is used for the detection of charged particle tracks, the measurement of their momenta and the determination of the event vertex. A momentum resolution of $\frac{\delta p}{p^2} \sim 0.3\%\ GeV^{-1}$ and an angular resolution of $\delta\vartheta$, $\delta\varphi < 1\ mrad$ is achieved for the reconstructed tracks. The dE/dx information from the drift chambers can also be used for particle identification. Besides, the tracking

system provides information which is used in the event trigger. The complete tracking system, as shown in figure 2.7, is divided into three parts: the forward tracker which is only used for the vertex reconstruction in this analysis, the central tracker and the backward drift chamber.

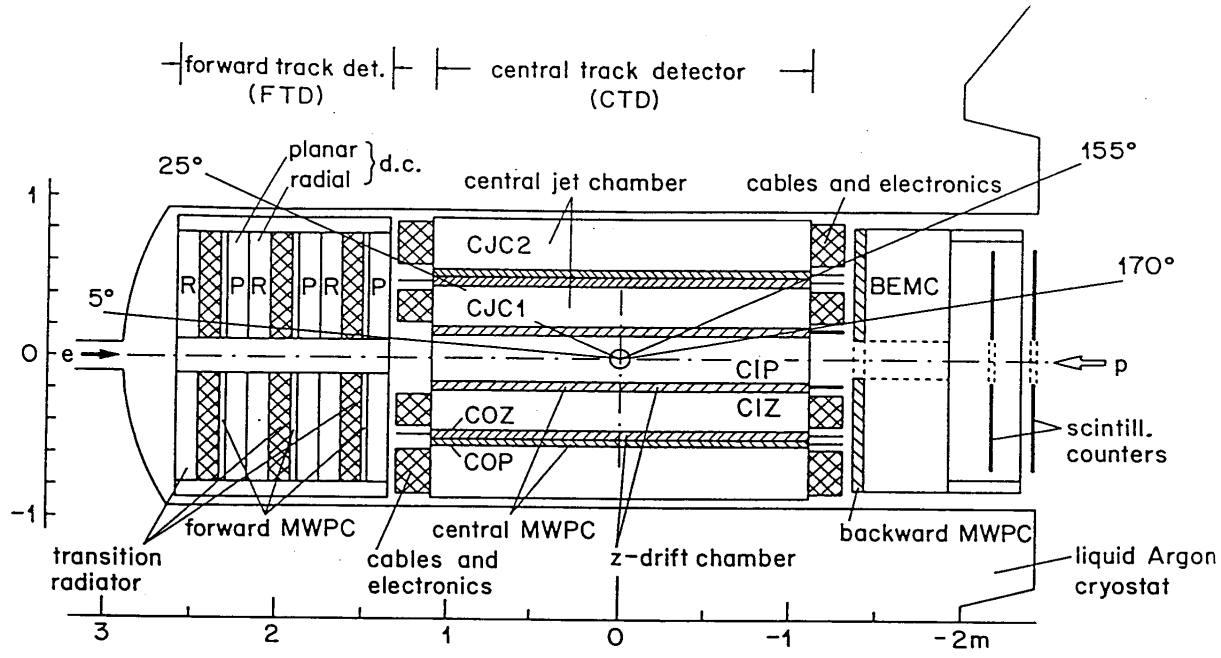

Figure 2.7: *Longitudinal view of the H1 Tracking System before the upgrade program of the backward region.*

2.3.1 The Central Tracking System

The central tracker is a combination of multiwire jet chambers, drift chambers and proportional chambers and covers an angular region between 25^o to 155^o.

The Central Jet Chambers (CJC1, CJC2)

These chambers work according to the following principles:

1. **Primary Ionization:** Incident charged particles are ionizing the gas atoms. If a produced electron has an energy above the ionization threshold ($E_{Ion} \sim 26\ eV$), it causes further ionization.

2. **Drift:** The motion of the electrons and the ions is controlled by applying an electric field (E) between the sense wires and the cathode wires. The produced

electrons drift towards the sense wires with a certain drift velocity depending on the gas used.

3. **Gas Amplification:** Near the sense wire, the electric field changes as $E \propto 1/r$ and reaches values of $E \sim 10^4 - 10^5\ V/cm$. As a result, the electron gains energy and new ions are produced. A large number of these ions near the sense wire produces an avalanche and amplifies the signal.

The central jet chambers are built from two cylindrical co-axial (the beam being the axis) jet chambers [8]. The inner one, CJC1 has a radial coverage from 20 cm to 45.2 cm, the outer one CJC2 from 52.7 cm to 85.5 cm and the cylinders are 220 cm long centered around the interaction point. chambers are filled with a mixture of Argon(Ar), Ethane(C_2H_4) and water(H_2O) in ratio 50 : 50 : 0.08 at atmospheric pressure in order to increase the primary ionization. The internal structure consists of sense wires, cathode wires, potential wires and field wires, all parallel to the beam. This allows to measure precisely the radial positions, but not the z-position of a track. As shown in figure 2.8, the wires form tilted planes at 30^o to the radial

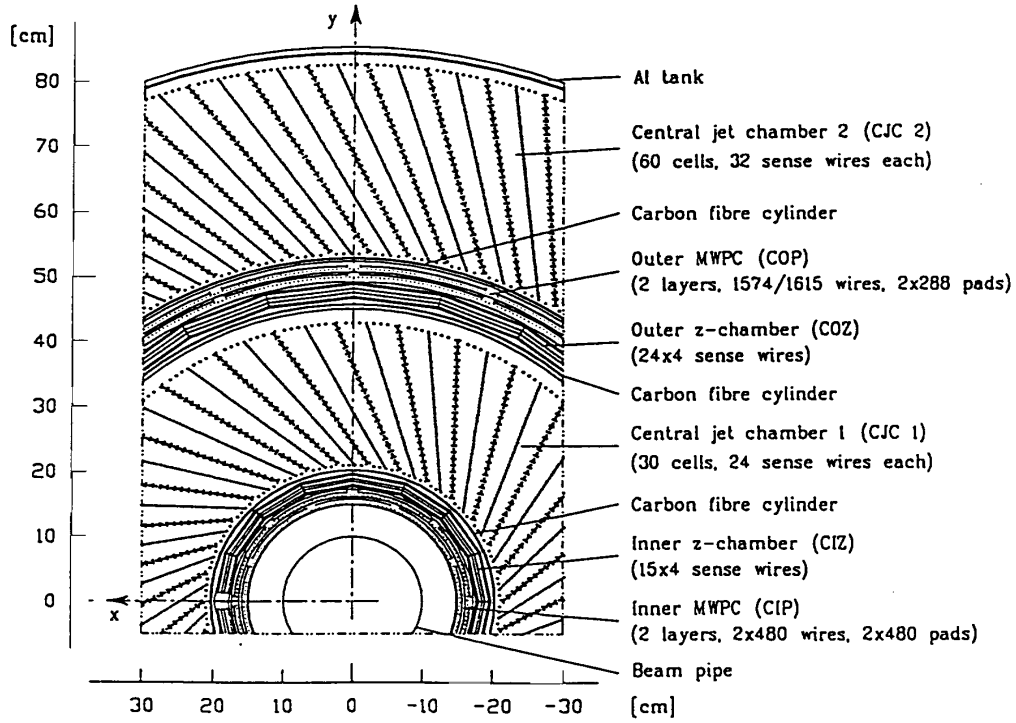

Figure 2.8: *The Central Tracking System, section perpendicular to the beam.*

direction. This tilt is provided to compensate the 30^o Lorentz angle in the presence of 1.2 T magnetic field so that in the presence of the high transverse momentum tracks, the drift direction is perpendicular to the field.

The above described wire geometry provides a nice transverse resolution of $\sigma_{r\varphi} \sim$ 170 μm. A rough estimation of the z-measurement is done by the charge division

method in which the sense wire currents are measured at both ends of the sense wires. This method gives a resolution of $\sigma_z \sim 2.2\ cm$ (i.e. 1% of the wire length). The resolution obtained in the energy loss measurement is $\sigma_{dE/dx} \sim 10\%$.

The Central z-Chambers (CIZ, COZ)

Due to the poor precision in the z-position determination of the CJC chambers, two additional chambers were added, the innermost CIZ, lies in front of CJC1 and the outer one COZ, in between CJC1 and CJC2 (See figure 2.8). The polar angles range covered by CIZ and COZ are $16^o < \vartheta < 169^o$ and $25^o < \vartheta < 156^o$ respectively.

1. CIZ: The chamber forms a 16 faces regular polygon in the cross-section with a thickness of 0.012 radiation length X_o. In the z-direction, the chamber is divided into 15 equal rings, each ring being drift cell 12 cm long and 2 cm thick, where the wires are mounted along polygons. The wire planes are tilted by 45^o with respect to the beam, tilted backward for the first 9 cells while tilted forward for the remaining 6 cells according to the direction of the crossing tracks. This wire geometry resolves the right-left ambiguity and it eliminates the dependence of the chamber resolution on the crossing angle.

2. COZ: The chamber cross-section is a 24-faces regular polygon. The number of cells and their azimuthal size is the same as in CIZ. The wire planes are not tilted and these planes are aligned perpendicular to the beam. Mirror tracks can be eliminated, as they do not point to the vertex.

In each cell, the soldering of the wires is performed at $\varphi = 0^o$ and amounts to a dead zone in φ of 7.7% of 2π for CIZ and 5.3% of 2π for COZ. The chambers allow for a precision of the measurement in z of $\sigma_z = 260\ \mu m$ for CIZ and $\sigma_z = 200\ \mu m$ for COZ, while the resolution in $r\varphi$, which is determined by the charge division at the wire ends, is rather poor ($\sigma_{r\varphi}$) of 28 mm and 58 mm respectively.

The Central Proportional Chambers (CIP, COP)

Next to the z-chambers, two thin cylindrical proportional chambers, CIP and COP (see figure 2.8) are located which give space points for three different triggers [9]. Combining these space point informations with the one from the four planes of the FPC (Forward proportional chambers) and those from the CIZ and the COZ allows for a fast estimation of z-vertex position. The system provides a good timing measurement for the particle tracks with a resolution of 75 ns for CIP and 60 ns for COP. By looking at their structure, the CIP is divided into sixty sectors in z-direction each of a width $\delta z = 3.65\ cm$ and in eight sectors in φ, each of a width $\delta\varphi = 45^o$ while the outer chamber COP, consists of 18 sectors in z-direction each with a width $\delta z = 12.1\ cm$ and sixteen sections in azimuthal direction with a width of $\delta\varphi = 22.5^o$.

2.3.2 The Forward Trackers

The angular acceptance for the forward trackers [10] (fig 2.7) is $7^o \leq \vartheta \leq 25^o$. The system is composed of three identical supermodules, which are the combination of planar and radial drift chambers and proportional chambers.

The Planar Modules

In the planar drift chambers the wires are parallel to each other (see figure 2.9) and the whole chamber is orthogonal to the beam. The system consists of three planes oriented at 0^0 and $\pm 60^0$, with a total of 1152 channels. The main purpose of the planars is the ϑ measurement with a resolution below 1 $mrad$. The radial resolution is of $150 - 170$ μm while the double track resolution is below 2 mm.

The Radial Modules

Three radial wire drift chambers [11, 12] are improving the $r\varphi$ and r reconstructions. The basic structure contains wire strung radially from $r = 15$ cm to $r = 76$ cm (see figure 2.9). Each radial consists of 48 wedge shaped drift cells in φ.

The Forward Proportional Chambers:

The Forward Proportional Chambers are giving a fast timing information which is used as a veto for interactions, which are produced out of the time-window of an ep collision. The information of a the presence of a signal in the forward tracker, assembled to a ray, is used in combination with the CIP/COP information in trigger elements indicating the presence of a vertex.

2.3.3 The Backward Drift Chamber

As stated earlier the former Backward Proportional Chamber (BPC) was replaced before the 1995 data taking by a Backward Drift Chamber (BDC) [15, 16]. The BPC was used to measure the impact points of the charged particles tracks in front of the BEMC with a precision of 1 mm. However, being a plane chamber it did not measure the direction and the momentum of the charged particles tracks. This measurement was performed by the central trackers but restricted in acceptance to $\vartheta < 165^o$ given by CJC1.

The newly installed backward drift chamber (BDC) covers the angular region of $153^o \leq \vartheta \leq 177.5^o$. The system (see figure 2.10) contains 4 parallel planes of double layers perpendicular to the z-axis, each plane has 8 equal azimuthal sectors with 44 radial wires per sector thus forming a cobweb geometry . The distance between two wires decreases as one goes from higher to lower radii, in order to cope with the high background rate (beam gas, beam wall) which increases as one goes closer to the beampipe. Each of the four planes is tilted with respect to its adjacent plane by 11.25^o so that the whole detector provides 32 effective φ segments, which are unique segments in 3-dimension. The detector contains the gas mixture of $92.5\% Ar, 5\%$

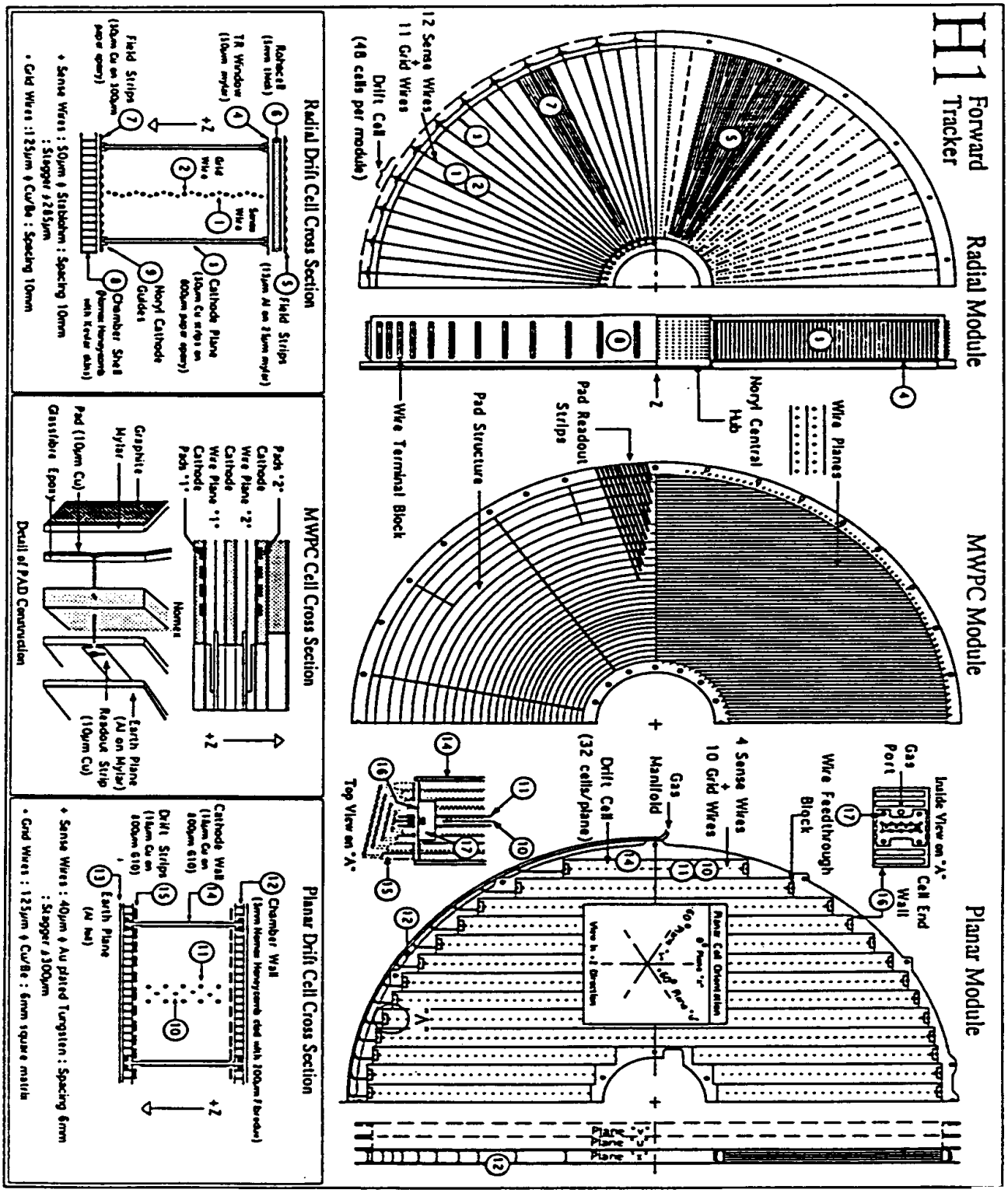

Figure 2.9: *The three different modules of the Forward Tracking System, section perpendicular to the beam and the corresponding cell structures.*

isobutane and $2.5\% NH_3$. The gas mixture provides a reasonable gas amplification factor of 5.10^4 and the drift velocity of ionization electrons is $v_d = 28\ \mu m/ns$ at $E = 1kV/cm$, directed radially.

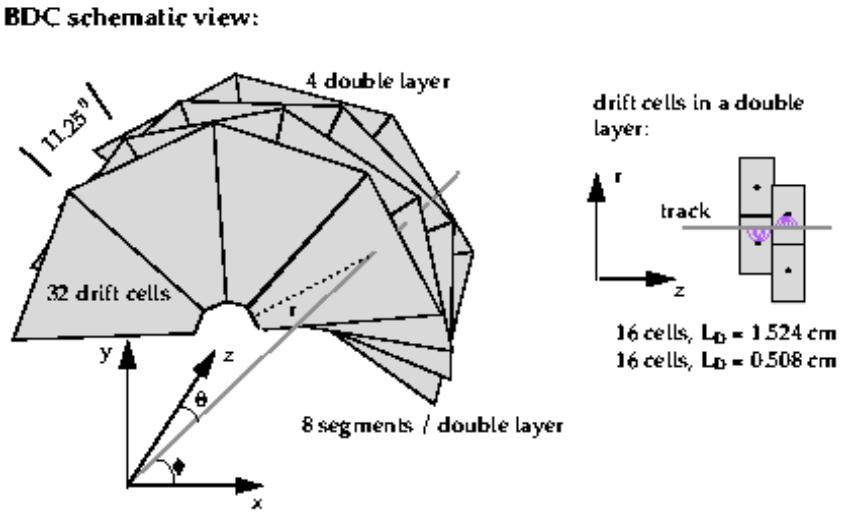

Figure 2.10: *Schematic view of the BDC, showing the arrangement of the 4 double layers and the structure of a double layer readout cell.*

The described BDC geometry provides an impact point with a good radial resolution of $\sigma_r \sim 0.4\ mm$ and an azimuthal resolution of $\sigma_\varphi \sim 0.8\ mm$ for non-showering particles while it has a moderate hit resolution of 400 μm in ϑ and 1 mm in φ. The double track resolution is 3 mm. There is a large amount of dead material in front of the BDC due to the CJC's end walls, electronics and cables with a variable depth from 0.5 to 2 radiation lengths with an inhomogeneous structure. This dead material produces preshowering of the electron in about 60 to 70% of the events. The BDC can measure the energy loss of the electron due to this preshowering by measuring dE/dx with a precision of $\sigma_{dE/dx} \sim 30\%$, but this has not been used for the analysis so far. In the case of showering particles the resolution degrades as $\sigma_r \sim 1.4mm$ and $\sigma_{r\varphi} >\sim 1.5mm$.

The Electron Track Reconstruction

The BDC is a vital detector in the backward direction in order to identify the electron in low Q^2 events. Therefore an electron candidate is only validated, if the electron cluster in the SpaCal can be associated to a track measured in the BDC. In order to use the maximum available information, from the track reconstruction one defines χ'^2 [15], adding to the usual χ^2 criteria, using the distance of the closest approach between tracks and hits, the difference between the electron cluster and a

BDC track,

$$\chi'^2 = \chi^2 + (\frac{\delta\vartheta}{\sigma_\vartheta})^2 + (\frac{\delta(d\varphi/dz)}{\sigma_{d\varphi/dz}})^2 \tag{2.2}$$

Here $\delta\vartheta$ is the difference in the polar angle of the track and the angle from the electron cluster to the vertex and $\delta(d\varphi/dz)$ is the difference in the corresponding slopes. For the electron reconstruction only 5 tracks with minimum χ'^2 are kept and the remaining tracks are rejected. Among these five tracks the electron is selected as one with a minimal projected distance from the SpaCal cluster.

The polar angle resolution depends upon the radial resolution, the resolution in z-vertex and the resolution in z-BDC. As the later two are very small, one can neglect them and hence

$$\sigma_\vartheta = \frac{\sigma_R}{z_{BDC} - z_{vtx}} \tag{2.3}$$

from which one finds a resolution of 0.6 $mrad$ for non-preshowering events. While comparing the data with the simulation, one finds a shift of 0.5 $mrad$ in the angular distribution which is included in the systematic errors for the F_2 measurement.

2.4 The Calorimeters

The tracking systems can only detect charged particles and as the resolution dp/p is proportional to p, the momentum measurement is more accurate for low momentum particles. For sampling calorimeters, where only a fraction of the deposited energy is detected by some active material, the energy resolution $\delta E/E$ varies as $1/\sqrt{E}$, therefore high energetic particles are more precisely measured with a calorimeter, whereas neutral particles can only be measured by the calorimeter. The energy loss as a function of the distance varies as $\sqrt{E}$ for a tracker, while for calorimeters it varies as $\log(E)$. This means that the calorimeters are very compact in order to absorb a particle, whereas trackers only modify slightly the trajectory of a particle. With a high granularity, calorimeters can determine the position of isolated particles and electromagnetic and hadronic particles can be separated by looking at the longitudinal and transverse structure of the measured shower.

5 In High Energy Experiments we use sampling calorimeters

The response time of calorimeters vary, depending on the active material. In the case of scintillators, the response is very fast and precise, as for example in the case of the SpaCal calorimeter, where the timing resolution is about 1 ns. For the liquid Argon Calorimeter, the response time is limited by the drift velocity of electrons in the liquid Argon and the rise time of the electronic signal. However the timing information of calorimeters is used to veto interactions out of the timing window in the trigger system, which is rejecting non-ep background events.

Electromagnetic Showers

A photon of a few MeV will interact with matter either by photoelectric or by Compton effect, while an electron of a few MeV interacts with the detector material

via ionization and excitation (Figure 2.11). At energies of several GeV the dominant process for photons is e^+e^- pair production and Bremsstrahlung for electrons. These interactions give rise to electromagnetic cascades.

The total longitudinal length, lateral radius and the starting point of the cascade formation depends on the material of the detector depend on the energy of the particle. One defines the radiation length X_o as the length of material through

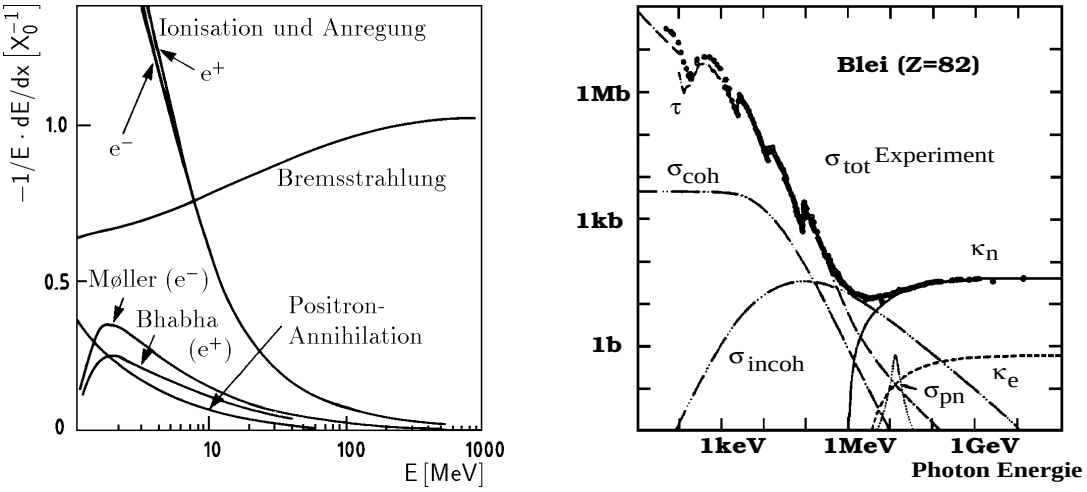

Figure 2.11: *Energy loss by a electron (left) and an photon (right) as a function of the energy in Lead.*

which an energetic electron looses $1 - e^{-1} \sim 67\%$ of its energy by Bremsstrahlung [17]. X_o depends strongly on the material, 5 X_o correspond for example to 45 cm of Al but less than 3 cm of lead, whereas the longitudinal shower development as a function of X_o is nearly independent of the material. For a 10 GeV electron the shower is generally contained in about $25X_o$ [18] The transverse development of an shower is expressed by the Molière radius ρ_M, which is defined as the transverse radius of a shower of an electron after one radiation length. About 95% of the energy of an electromagnetic shower are contained in a cylinder of radius $r = 2\rho_M$, which corresponds to about 3.4 cm for lead.

Hadronic showers

In the formation of the hadronic showers, the interaction between the hadrons and the nuclei of the absorbing material has to be considered in addition [19]. Contrary to the electromagnetic showers, not all the energy of the hadron deposited in the detector can be measured since the energy involved in the breaking up of the interacting nucleons has to be taken into account. This can be compensated either by the choice of the absorbing material [20] or by software reweighting techniques, as performed by H1 [21]. In the case of hadronic showers, one defines the interaction length λ, as the length of the absorbing material through which a hadronic particle looses in average 67% of its energy. For the lateral extension of a hadronic shower,